

ATMOSPHERIC EFFECTS ON THE UTILITY OF SOLAR POWER ON MARS

**ROBERT M. HABERLE, CHRISTOPHER P. McKAY, and
JAMES B. POLLACK**
NASA Ames Research Center

OWEN E. GWYNNE
SETI Institute

DAVID H. ATKINSON
University of Idaho

JOSEPH APPELBAUM
Tel Aviv University

GEOFFREY A. LANDIS
Sverdrup Technology

RICHARD W. ZUREK
Jet Propulsion Laboratory

and

DENNIS J. FLOOD
NASA Lewis Research Center

Solar power is likely to play an important role in the coming exploration of Mars. As a resource it is cheap, in great supply, easy to convert into useful work, and lacks dangerous failure modes that can jeopardize the safety of future human outposts. Yet Mars is farther from the Sun and it has an atmosphere. In particular, dust storms are a major concern because they can literally envelop the entire planet, and can last for several months. Engineering studies of solar-powered systems designed to operate on the surface of Mars must carefully consider these aspects of the Martian environment. This chapter summarizes what is known about the Martian atmosphere as it relates to solar radiation at the surface. Thus, the composition of the atmosphere is reviewed and the gases and aerosols that affect the solar beam are identified and characterized, including dust particles and water ice clouds. A methodology is presented that enables the calculation of solar radiation at the surface. It is shown that although the presence of dust reduces the available energy, there still remains an appreciable diffuse component that can be utilized by solar collectors. Water-ice clouds have the same effect, but

are of less concern than dust particles because of their generally lower optical depths, and greater scattering ability. It is estimated that the power requirements of a human outpost located at the Viking Lander 1 site (23°N) could be met with solar arrays about 30 by 30 m square, and about 1000 kg in mass. A system somewhat less than twice that size and mass could meet the power requirements for *in-situ* propellant production as envisioned in the “Mars Direct” scenario as proposed by Baker and Zubrin (1990). Thus, solar power is a viable energy source for future missions to Mars.

I. INTRODUCTION

Solar energy is likely to be an important power source for surface-based operations on Mars. As a resource it is economical, in great supply, and the photovoltaic cells needed to convert it to useful work offer many advantages over conventional systems. For example, they are robust, require minimal maintenance, gracefully degrade, and can sustain considerable damage before losing their utility. These characteristics are particularly important for human outposts where safety is the major design requirement.

However, the design of solar-powered systems for Mars must consider the attenuating effects of its atmosphere. The Martian atmosphere, though thin in comparison with Earth's, does contain gases and aerosols that can attenuate the solar beam. Dust storms, for example, are known to produce visible optical depths of 5 or more—enough to completely block the Sun from view. However, because dust particles scatter as well as absorb solar radiation, there will be a diffuse component which can be significant (Appelbaum and Flood 1989*a, b*; Geels et al. 1989; Landis and Appelbaum 1990).

There are three goals for this chapter. The first is to review what is known about the Martian atmosphere as it relates to the deposition of solar energy at the surface. This includes a review of the abundance, distribution, properties, and variability of the principal optically active constituents: gases, dust particles, and water ice clouds. The second goal is to determine the effect of the atmosphere on the transmission of sunlight to the surface, and how that transmission varies with season, latitude, and time of day. The main concern is the effect of dust. Where possible, the spectral dependence of atmospheric transmissivity will also be discussed. Finally, the third goal is to assess the implications of the availability of sunlight at the Martian surface for the design of solar-powered surface systems. This will include a review of the state-of-the-art of solar cell technology, a power system analysis of a hypothetical human outpost, and a resource-processing application.

II. THE MARTIAN ATMOSPHERE

A. Gases

The principal gaseous constituents of the Martian atmosphere and their relative abundances by volume are listed in Table I. Of these, water vapor, ozone, and dust are variable. Together, these gases exert a mean pressure at the surface of

6.1 mbar which fluctuates seasonally by about 25% due to the condensation and sublimation of CO₂ in the polar regions. It is worth noting that ozone, which can absorb ultraviolet radiation, tends to be anti-correlated with water vapor. Water vapor in the lower atmosphere is photolyzed into H and OH which then participate in a catalytic cycle that destroys ozone (see, e.g., McElroy and Donahue 1972; Parkinson and Hunten 1972). Thus, regions of low water abundance can support large ozone concentrations. Ozone abundances as high as 60 μm atmospheres ($1 \mu\text{m atm} = 2.69 \times 10^{15}$ molecules cm^{-2}) have been observed near the edge of the north polar cap during winter (Barth 1985). Typical global-mean abundances, however, are less than several $\mu\text{m atm}$.

TABLE I^a

Composition of the Martian Atmosphere		
CO ₂	95.3%	
N ₂	2.7	
Ar	1.6	
O ₂	0.13	
H ₂ O	0.03 ^b	
CO	0.07	
Ne	2.5	ppm
Kr	0.3	ppm
Xe	0.08	ppm
O ₃	0.03	ppm ^b
Dust	10	ppm/m ^b

^a Table from Owen et al. 1977.

^b Variable.

B. Dust Particles

Background Levels. Dust particles may always be present in the Martian atmosphere. During the Viking mission, the solar optical depth was measured at the two Viking Lander sites for 1 1/3 Mars years (Fig. 1). At no time did the optical depth fall below 0.18. During the relatively clear periods, the optical depth was typically 0.2 to 0.5. It is not clear how representative these values are because the Viking Lander sites are located in low-lying plains and may therefore see more dust in the overlying column. Furthermore, storm activity is suppressed in some years so that even lower values are possible. To be conservative, optical depths of 0.1 to 1.0 should be considered typical for those of the background dust haze.

The spatial distribution of the background haze is also uncertain. Modeling studies suggest that dust particles tend to become uniformly mixed with height (Haberle et al. 1982; Murphy et al. 1990) which is consistent with twilight observations at the Viking Lander sites (Kahn et al. 1981). Light profiles of the Martian limb indicate that a typical depth of the background

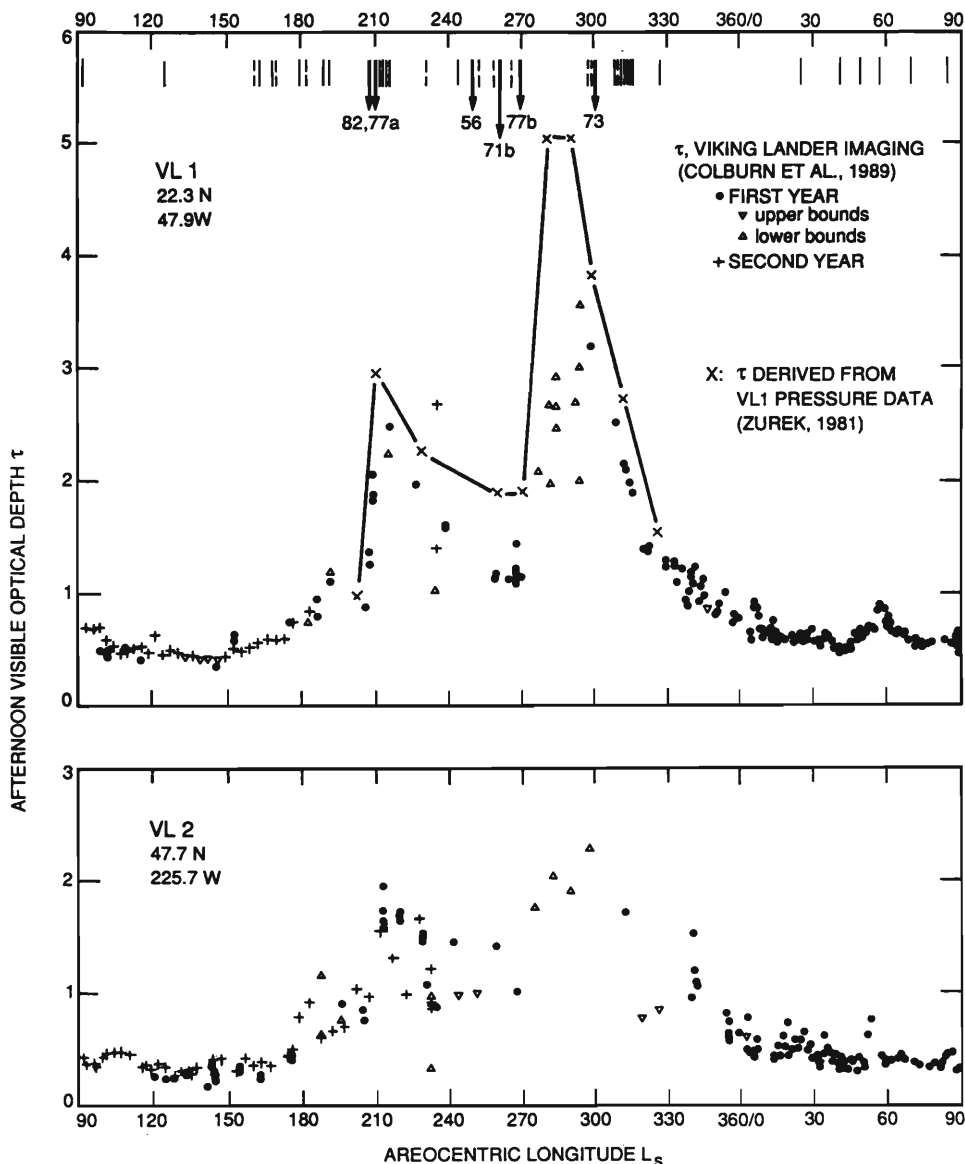


Figure 1. Visible optical depths derived from the Sun-diode measurements made at the two Viking Lander sites for more than 1 Mars year (from Colburn et al. 1989). The seasonal date on the abscissa covers one Mars year, as denoted by areocentric longitude, L_s . During the two planet-encircling dust storms in 1977, opacities were so large that only upper bounds could be estimated. Line indicates the opacity of a global haze inferred from Viking Lander 1 surface pressure data (Zurek 1981). Initial appearance or detection of all observed regional dust clouds, hazes or obscurations (vertical lines) and of planet-encircling (arrows) dust storms (Martin and Zurek 1993) are indicated at the top of the upper panel. Figure taken from Kahn et al. (1992).

haze is ~ 30 km, but that it can vary in latitude and season and may extend as high as 50 km (Jaquin et al. 1986).

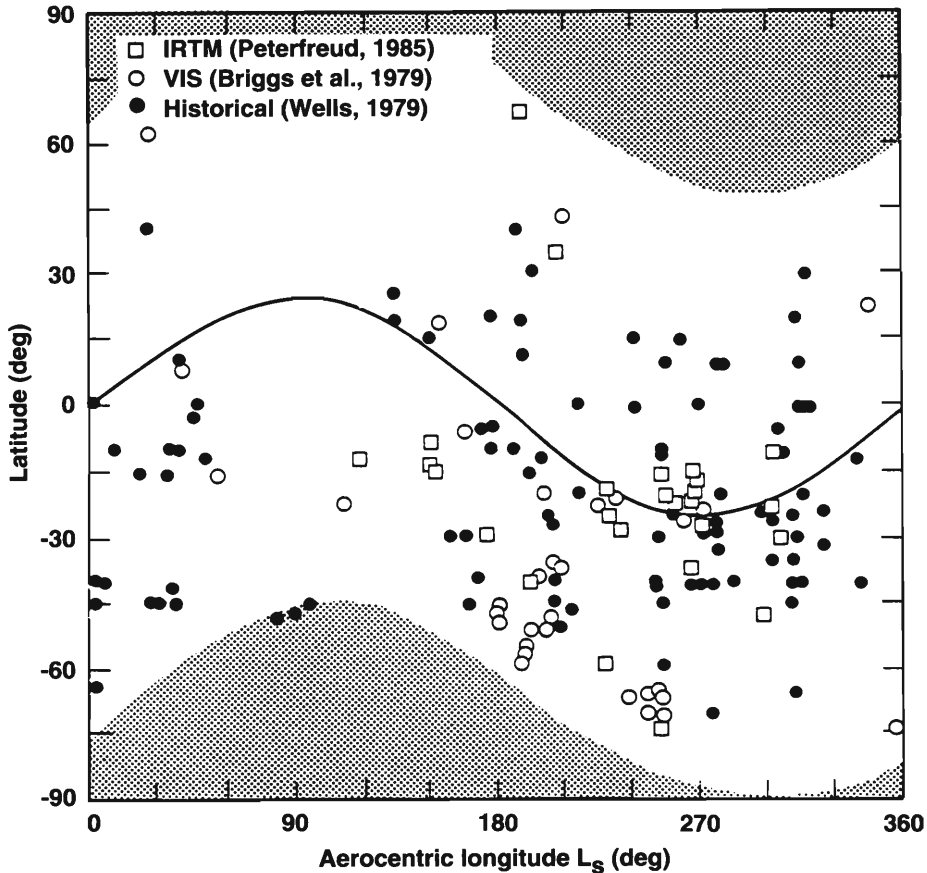


Figure 2. Latitude and time-of-year occurrence of local dust storms detected by the Viking Orbiters, from either infrared or visible imaging observations, and those observed from Earth, as compiled by Wells (1979). Taken from Peterfreund (1985).

Dust Storms. Dust particles are lifted into the Martian atmosphere by storms which range in size from local ($<10^5 \text{ km}^2$) to global ($\sim 10^8 \text{ km}^2$). Local storms are more frequent and may develop anywhere on the planet at any time of year. Our understanding of the frequency and distribution of local storms comes from the telescopic and Viking records which are limited in spatial and temporal coverage. The results of these observations are shown in Fig. 2. Although not pronounced, there is a tendency for these storms to cluster about the sub-solar point, and along the edge of the retreating south polar cap during spring. Based on the Viking results, approximately 100 local dust storms may occur each Martian year (Peterfreund 1985). Optical depths produced by these storms can be quite substantial ranging from 1 to 6 (Hunt 1979). Even higher values can be expected in localized regions. Local storms typically last a few days.

Occasionally, local storms can expand into regional (confined to a hemisphere and a region), or planet-encircling (covering both hemispheres) storms. Planet-encircling storms can be truly global in extent. Six such global dust storms have been observed (Table II). Of these, the 1971 storm was the longest, lasting for several months and completely obscuring the surface from view. In general the bigger the storm, the longer it lasts. Initial decay times for the two global dust storms observed by Viking in 1977 (Fig. 1) were 50 to 75 days (Pollack et al. 1977). A complete review of the characteristics of these great dust storms can be found in Zurek (1982).

TABLE II
Well-Documented Planet-Encircling Dust Storms

Year	L_s	Initial Location	Observation
1956	250°	30°S 31°E	Telescopic
1971	260°	29°S 38°E	Telescopic/Mariner 9
1973	300°	24°S 88°W	Telescopic
1977	204°	30°S 70°W	Viking
1977	268°	?	Viking
1982	200°	?	Viking

Optical depths during planet-encircling storms are likely to be highly variable in space and time. At the Viking Lander sites, only lower limits on the peak opacity could be estimated because the Sun was obscured by dust. Theoretical estimates have been made using the amplitude of daily pressure variations as a proxy for opacity (Zurek 1981). Such variations are sensitive to atmospheric heating and, hence, the global dust loading. Values as high as 6 have been determined using this method.

Unlike local storms, planet-encircling storms tend to develop from specific locations at specific seasons: the southern subtropics, during spring and summer (fall and winter in the north). The Hellas and Argyre basins, along with Noachis and Solis Planum, are the most active regions. At this season and latitude, the available solar radiation is near its maximum yearly value and the strength of the general circulation is high (Pollack et al. 1990). However, planet-encircling storms do not occur each Martian year (Martin and Zurek 1993; Zurek and Martin 1993). During the Viking mission, they were observed during the first and fourth year of observations, but not during the second and third years. Since then, no dust storms greater than regional in size have been observed. Prior to the era of spacecraft exploration, only one planet-encircling storm—the 1956 storm—was observed. From observations at all favorable oppositions since 1905, one concludes that planet-encircling storms may be episodic. However, the possibility that such storms went unobserved at other times cannot be ruled out. A summary of the occurrence of major dust storms since 1905 is given in Fig. 3.

Particle Properties. Because no *in-situ* measurements of dust particles in

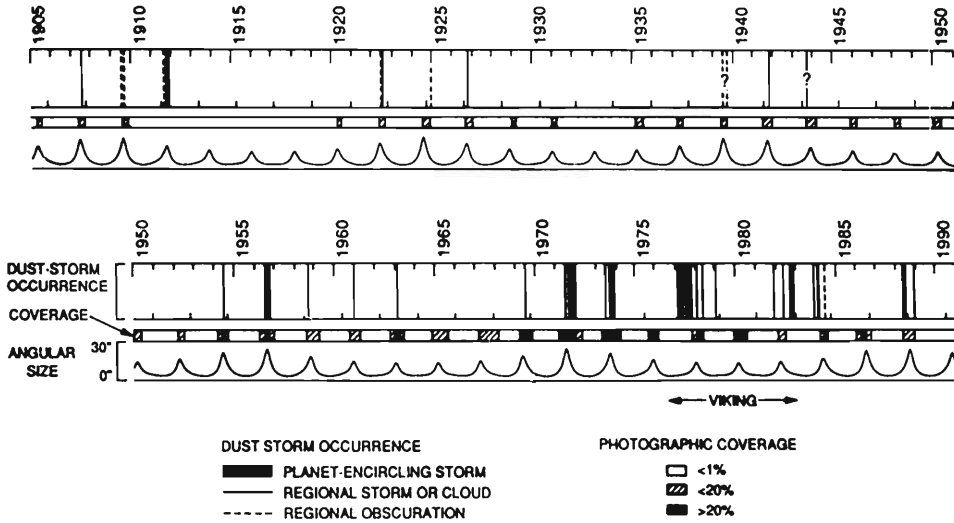


Figure 3. Time line of observed major dust storms on Mars (Zurek and Martin 1993).

the Martian atmosphere have been made, their composition, size distribution, and shape are not well constrained. Instead, inferences about these characteristics are based on remote sensing measurements which cannot uniquely separate the various contributions to the observed opacity. Synthesized thermal emission spectra of the 1971 global dust storm compare favorably with the observed spectra for particles dominated by igneous silicates, or weathering products like clays. Some basalt may also be present. Relatively high SiO_2 contents ($>60\%$) have been inferred from these data (Hanel et al. 1972)—in contrast to the lower silicate abundance ($\sim 40\%$) inferred from soil measurements at the Viking Lander sites (Toulmin et al. 1977; Clark et al. 1982). The density of silicate materials on Earth is typically 2 to 3 g cm^{-3} and is probably a good estimate for Martian dust densities as well.

The synthesized spectra also imply a particle size distribution having a mode radius of $0.4 \mu\text{m}$, and a cross-section weighted-mean radius of $2.5 \mu\text{m}$ (Toon et al. 1977). Using this size distribution, a density of 3 g cm^{-3} , and assuming the dust particles are uniformly mixed with a scale height $H = 10 \text{ km}$, the concentration of dust particles as a function of height z can be approximately obtained from

$$N \sim N_0 \tau \exp(-z/H) \quad (1)$$

where $N_0 = 6 \text{ cm}^{-3}$ is the number density at the surface when the optical depth $\tau = 1$. Thus, during a major dust storm ($\tau = 5$) there are approximately $30 \text{ particles cm}^{-3}$ at the surface. It should be noted, however, that this estimate is sensitive to the assumed particle size distribution. Other distributions with cross-sectional mean radii ranging from $0.4 \mu\text{m}$ (Pollack et al. 1977; Clancy and Lee 1991) to $10 \mu\text{m}$ (Leovy et al. 1972) have been estimated. These distributions imply that N_0 varies between 38 and $1.5 \text{ particles cm}^{-3}$.

Thus, there is significant uncertainty in actual concentrations. In addition, concentrations can be much higher in regions of active dust raising. In this sense, Eq. (1) can be regarded as a lower limit.

The dust loading of the atmosphere can also be estimated though it is subject to the same uncertainties as the concentration. For a $2.5\ \mu\text{m}$ mean particle radius, Pollack et al. (1979) show that the mass loading (g cm^{-2}) is related to the optical depth by

$$m = 5.0 \times 10^{-4} \tau \quad (2)$$

Thus, a column with unit optical depth contains about $5 \times 10^{-4}\ \text{g cm}^{-2}$ of dust—enough to form a layer $\sim 2\ \mu\text{m}$ thick. During a global dust storm there is an equivalent of $\sim 10\ \mu\text{m}$ of dust in the atmosphere. Thus, the amount of dust that settles out of the atmosphere following a single storm may be quite small. This is consistent with changes in the surface brightness seen by the Viking Landers (Arvidson et al. 1983). However, it may have a significant effect on the performance of solar cells (see Sec. V).

TABLE III
Dust Particle Single Scattering Properties

Wavelength, μm	ω_o	g	Q_{ext}
0.35	0.598	0.736	3.052
0.40	0.627	0.682	3.177
0.45	0.659	0.634	3.294
0.50	0.695	0.592	3.40
0.556	0.735	0.556	3.48
0.669	0.840	0.497	3.58
0.80	0.901	0.492	3.30
1.0	0.739	0.585	2.50
Solar Average ^a	0.751	0.576	3.06

^a Weighted by the solar spectrum and the products integrated over wavelength.

The shape of Martian dust particles is also uncertain. Sky brightness measurements from the Viking Lander sites suggest the particles are non-spherical but equidimensional (Pollack et al. 1977). In addition, disk-shaped particles, because they settle out of the atmosphere more slowly are better able to reproduce several observed characteristics of dust particles in the Martian atmosphere (Murphy et al. 1993). These characteristics include the relatively small temporal variation in the particle size distribution (Toon et al. 1977), and the small temporal and spatial variation of the visible-to-infrared opacity (Martin 1986). However, the latter can also be reproduced with spherical particles, though not uniquely (Clancy and Lee 1991). In the absence of more definitive measurements, the particle shape remains uncertain.

Radiative Properties. The size and composition of Martian dust particles permits them to interact efficiently with solar radiation. That interaction can be quantified given knowledge of the particles' single scattering properties and optical depth. The latter has been directly measured by the Viking Landers (Colburn et al. 1989); the former have been estimated from the angular variation of sky brightness (Pollack et al. 1979). The single scattering properties of interest are the single-scattering albedo ω_o , the particle asymmetry factor g , and the extinction efficiency Q_{ext} . The values of these parameters for each of the six different filters on the Lander cameras, as well as their solar average value, are listed in Table III.

B. Water-Ice Clouds

Occurrence and Distribution. Water vapor in the Martian atmosphere is controlled by saturation so that clouds are fairly common. They have been observed as wave clouds, convective clouds, ground fogs, high altitude hazes, and the so called "polar hood" (Leovy et al. 1972,1973; Briggs and Leovy 1974; French et al. 1981; Kahn 1984). However, the water content of Martian clouds is much less than their terrestrial counterparts because of the colder thermal environment. Consequently, optically thick clouds on Mars are less widespread than they are on Earth.

In general, Martian clouds appear to form more frequently in the northern hemisphere than in the southern hemisphere, and during fall and winter rather than spring and summer. This is especially true of the polar hoods which appear as deep (~ 10 km) polar-encircling fogs. This asymmetry is related to the fact that the north residual cap is water ice (and therefore acts as a source for atmospheric water) while the south residual cap is CO_2 ice (and therefore acts as a sink for atmospheric water). In addition, clouds form more easily at high latitudes than at low latitudes because saturation is more readily achieved. The exception is the upland regions of Tharsis during northern summer when frequent convective clouds resembling fields of large diffuse cumulus have been observed. Also, ground fogs have been observed in tropical craters and canyons but because they sublimate well before noon, they are not an issue for solar power. Some high-altitude tropical hazes may also be diurnally varying (Colburn et al. 1989)

Physical and Radiative Properties. Very little is known about the physical properties of Martian clouds. Spectral measurements of a single cloud indicate particles in the μm -size range (Curran et al. 1973). On theoretical grounds, a variety of particle sizes are expected depending on altitude, dust loading, humidity, etc. (Kahn 1990). Higher clouds generally contain smaller particles and are less opaque than lower clouds. Estimates of the mean particle size (radius) range from sub- μm for the high clouds, to several μm for the low clouds. The corresponding visible opacities range from near 0 to about 0.5, though higher values are certainly possible.

Without knowledge of the particle shape and size distribution the single scattering properties of Martian clouds cannot be determined. However, it

is likely that they are fairly conservative ($\omega_o \sim 1$) and moderately forward scattering ($g \sim 0.6$). In estimating the transmission properties of Martian clouds, we have adopted these values as a first approximation.

III. ATMOSPHERIC EFFECTS ON SOLAR TRANSMISSION

A. Solar Radiation at Mars

The first step in the assessment of solar power on Mars is to determine the maximum amount of sunlight S available at a given location, season, and time of day. S is therefore the irradiance of solar radiation incident on the top of the atmosphere. It can be calculated from

$$S = \mu S_0 \left(\frac{\bar{r}}{r} \right)^2 \quad (3)$$

where $\mu = \cos z$ is the cosine of the solar zenith angle z ,

$$\cos z = \sin \theta \sin \delta + \cos \theta \cos \delta \cos h. \quad (4)$$

$S_0 = 590 \text{ W m}^{-2}$ is the solar irradiance at Mars' mean distance from the Sun \bar{r} ($= 1.52 \text{ AU}$), θ and δ are the latitude and solar declination, $h = 2\pi t/P$ is the hour angle, t is time measured from local noon, and $P = 88775 \text{ s}$ is the length of the Martian solar day. The solar declination angle depends on Mars' obliquity ϵ ($25^\circ.2$) and orbital position L_s . The latter is an angular measure: $L_s = 0^\circ$ corresponds to northern vernal equinox; $L_s = 90^\circ$ corresponds to northern summer solstice, and so on. The solar declination angle is related to ϵ and L_s by

$$\sin \delta = \sin \epsilon \sin L_s. \quad (5)$$

Finally, the Sun-Mars distance r can be found from

$$\left(\frac{\bar{r}}{r} \right) = \frac{1 + e \cos(L_s - L_s^p)}{1 - e^2} \quad (6)$$

where $e = 0.0934$ is the orbit eccentricity, and $L_s^p = 250^\circ$ is the areocentric longitude at perihelion. It is worth noting that the high eccentricity of Mars' orbit results in a significant seasonal variation in the available solar irradiance. At perihelion the maximum available irradiance is $S = 717 \text{ W m}^{-2}$, while at aphelion the maximum is $S = 493 \text{ W m}^{-2}$. This is a much greater variation than experienced on Earth.

A useful quantity is the daily averaged insolation \bar{S} . Integrating Eq. (3) from Sunrise to Sunset gives

$$\bar{S} = \frac{S_0}{\pi} \left(\frac{\bar{r}}{r} \right)^2 [\cos \delta \cos \theta \sin H + H \sin \delta \sin \theta] \quad (7)$$

where H is the half-day length (radians) which can be found from

$$\cos H = \begin{cases} -1, & \theta > \pi/2 - \delta \text{ or } \theta < -\pi/2 - \delta \\ -\tan \theta \tan \delta, & |\theta| < \pi/2 - |\delta| \\ +1, & \theta > \pi/2 + \delta \text{ or } \theta < -\pi/2 + \delta \end{cases} \quad (8)$$

Note that $\cos H = -1$ when the Sun never sets, and $\cos H = +1$ when it never rises.

The daily averaged insolation as a function of latitude and season is shown in Fig. 4. Maximum insolation occurs at the poles where the increased day length more than compensates for the low zenith angles. The south pole has a higher seasonal maximum than the north pole because southern summer occurs near perihelion. Of course solar-powered systems would not be able to provide continuous power all year long at these latitudes because of the long polar nights. At the equator, however, seasonal variations are small and continuous power is possible all year long.

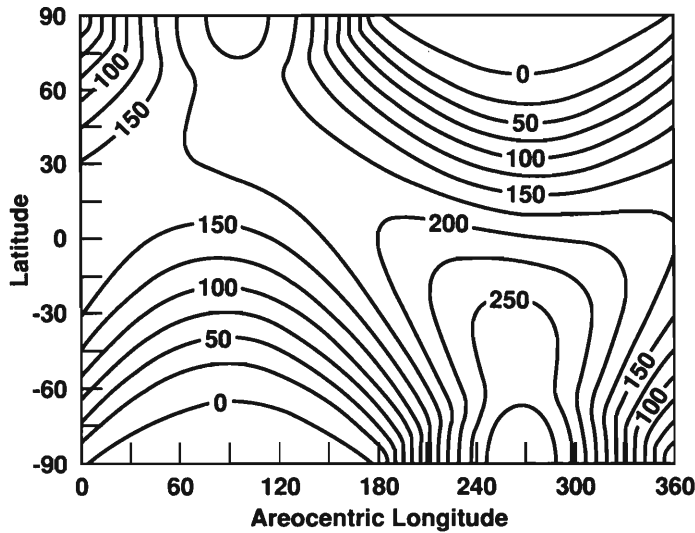


Figure 4. Daily averaged solar insolation at the top of the atmosphere. Contour intervals are 25 W m^{-2} .

The annually averaged insolation as a function of latitude is given by

$$\langle \bar{S} \rangle = \frac{S_0}{2\pi^2} (1 - e^2)^{\frac{1}{2}} \int_0^{2\pi} [1 - (\sin \theta \cos \epsilon - \cos \theta \sin \epsilon \sin \lambda)^2]^{\frac{1}{2}} d\lambda \quad (9)$$

where the integration is over all longitudes λ . $\langle \bar{S} \rangle$ is a maximum at the equator and is hemispherically symmetric (Fig. 5). However, due to the eccentricity

of Mars' orbit, the maximum and minimum of \bar{S} are not symmetric; the minimum is sharply peaked in latitude, whereas the maximum is not. The highest minimum occurs at 15°N , while the lowest maximum occurs over a broad range of latitudes between 30 to 60°N . Thus, the low latitudes of the northern hemisphere experience the least seasonal variation, while the high latitudes of the southern hemisphere experience the greatest seasonal variation.

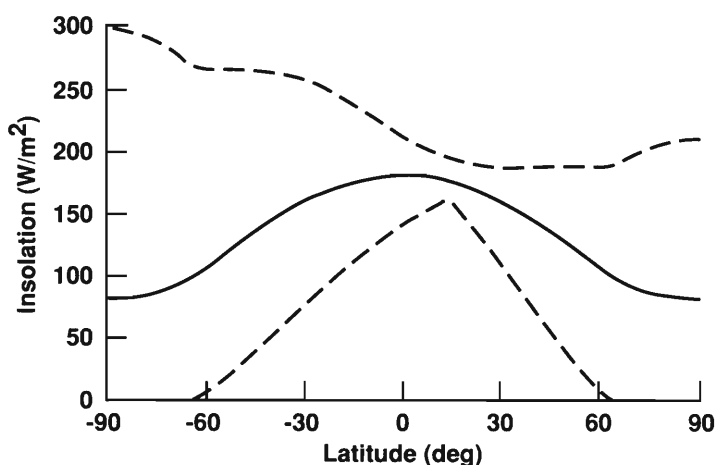


Figure 5. Mars annual insolation. At each latitude, the daily averaged insolation varies during the course of the year. Maximum (top dashed), minimum (bottom dashed), and mean (middle solid) daily averaged insolation are illustrated in this figure.

B. Atmospheric Extinction

Gases. Kuhn and Atreya (1979) have discussed the molecular extinction of solar radiation on Mars. Of the gases listed in Table I, CO_2 , H_2O , O_2 , and O_3 are of most interest. Except in the far ultraviolet, scattering by these gases contributes very little to the total extinction which is dominated instead by absorption. The effectiveness of these gases as absorbers is given by the product of their column density and absorption cross section. Their approximate time and globally averaged column densities (molecules cm^{-2}) are $[\text{CO}_2] = 2 \times 10^{23}$, $[\text{H}_2\text{O}] = 4 \times 10^{19}$, $[\text{O}_2] = 10^{20}$, and $[\text{O}_3] = 5 \times 10^{15}$. From 200 to 1500 nm the absorption cross section for CO_2 is negligible (Banks and Kockarts 1973) and radiation at these wavelengths undergoes very little absorption by this gas. Water vapor on the other hand, has many absorption features in this region, but is too scarce ($<10^{-3}$ of that found on Earth) to affect much absorption. This is also true for O_2 and O_3 . Consequently, there is very little molecular absorption of radiation between 200 and 1500 nm in the Martian atmosphere. Shortward of 200 nm, however, the CO_2 cross sections become large enough ($>> 5 \times 10^{-24} \text{ cm}^2$) to yield significant opacity. Water vapor and O_2 also begin to absorb shortward of 200 nm, but their contribution

is small compared to the more abundant CO_2 . In any case, virtually no radiation at wavelengths <200 nm reaches the Martian surface.

That part of the ultraviolet irradiance that does reach the surface (200–350 nm) constitutes about 4.5% of the total solar energy. Therefore, the distribution of incident ultraviolet radiation at the surface can be found by multiplying 0.045 times the value shown in Fig. 5. Exceptions to this occur when the ozone column density departs significantly from the time and globally averaged value quoted above. Such departures occur mainly near the edge of the winter polar cap where column densities as high as 150×10^{15} molecules cm^{-2} have been observed (Barth 1985). As the absorption cross section for O_3 is 10^{-17} cm^2 at 260 nm (Daumont et al. 1983), such concentrations can produce a measurable opacity. However, the solar zenith angle is so large in this situation that very little solar energy is available anyway (at least for horizontal collectors). In the summer hemisphere and at midlatitudes, O_3 concentrations are typically $<5 \times 10^{15}$ molecules cm^{-2} and very little attenuation of ultraviolet radiation occurs.

In general, therefore, a clear Mars atmosphere is transparent to solar radiation at wavelengths >200 nm, and opaque to solar radiation at wavelengths <200 nm. If the atmosphere is dusty, however, additional near-ultraviolet opacity could be provided. Indeed, if the ultraviolet opacity is comparable to the visible opacity (as would be theoretically expected because the particles are much larger than ultraviolet wavelengths), then dust could be the greatest source of opacity in this region of the spectrum. Ultraviolet reflectance measurements are consistent with this interpretation (Hord et al. 1972). However, in the absence of more definitive measurements, damage due to radiation in the 200 to 350 nm region should be considered an issue for solar collectors and other equipment exposed on the Martian surface.

Dust. The main concern for solar-powered systems is the effect of suspended dust particles on the amount of sunlight reaching the surface. These effects can be calculated given the particles' single scattering properties discussed earlier. Pollack et al. (1990) have used these properties in a doubling/adding code to calculate the net irradiance as a function of altitude, total optical depth, surface albedo and zenith angle. The results were stored in a four-dimensional look-up table which was intended to speed up heating rate calculations in a general circulation model. For solar power studies, however, it is the total downward irradiance—not the net irradiance—that is of interest. The total downward irradiance, F_{tot} , can be obtained from the Pollack et al. data using the following formula

$$F_{\text{tot}} = \frac{Sf(\tau, \mu, A)}{(1 - A)} \quad (10)$$

where A is the surface albedo, and $f(\tau, \mu, A)$ is a normalized net irradiance function whose value as a function of optical depth and zenith angle is given in Tables IV and V. Previous studies of solar power on Mars have utilized

TABLE IV
 Normalized Net Irradiance Function for a Surface Albedo = 0.1

Optical Depth, τ	Solar Zenith Angle, Degrees									
	0	10	20	30	40	50	60	70	80	85
0.100	0.883	0.883	0.881	0.879	0.875	0.868	0.855	0.830	0.757	0.640
0.200	0.866	0.865	0.862	0.857	0.850	0.836	0.813	0.768	0.651	0.508
0.300	0.848	0.847	0.842	0.835	0.826	0.806	0.773	0.712	0.571	0.433
0.400	0.830	0.829	0.823	0.814	0.801	0.776	0.736	0.663	0.510	0.385
0.500	0.813	0.811	0.804	0.793	0.778	0.748	0.701	0.619	0.462	0.351
0.600	0.796	0.793	0.785	0.772	0.755	0.721	0.668	0.579	0.422	0.325
0.700	0.778	0.775	0.766	0.752	0.732	0.695	0.638	0.546	0.393	0.306
0.800	0.761	0.758	0.748	0.732	0.711	0.670	0.609	0.514	0.366	0.288
0.900	0.744	0.741	0.730	0.713	0.690	0.646	0.583	0.486	0.345	0.274
1.000	0.728	0.724	0.712	0.694	0.669	0.623	0.557	0.459	0.324	0.261
1.100	0.712	0.708	0.696	0.676	0.649	0.602	0.535	0.438	0.309	0.250
1.200	0.695	0.691	0.679	0.658	0.630	0.581	0.513	0.416	0.295	0.240
1.300	0.679	0.675	0.662	0.640	0.611	0.560	0.491	0.395	0.280	0.230

1.400	0.664	0.660	0.646	0.624	0.594	0.542	0.473	0.379	0.270	0.222
1.500	0.649	0.644	0.630	0.607	0.576	0.524	0.455	0.364	0.260	0.215
1.600	0.634	0.629	0.615	0.591	0.559	0.506	0.437	0.348	0.249	0.207
1.700	0.619	0.614	0.599	0.575	0.542	0.489	0.420	0.333	0.240	0.200
1.800	0.605	0.600	0.585	0.561	0.527	0.475	0.460	0.321	0.232	0.194
1.900	0.591	0.586	0.571	0.546	0.513	0.460	0.392	0.310	0.225	0.188
2.000	0.578	0.572	0.557	0.532	0.498	0.445	0.377	0.298	0.217	0.182
2.250	0.544	0.539	0.523	0.498	0.463	0.411	0.346	0.272	0.200	0.168
2.500	0.514	0.509	0.493	0.467	0.432	0.381	0.319	0.252	0.187	0.157
2.750	0.483	0.478	0.462	0.436	0.401	0.352	0.293	0.231	0.173	0.146
3.000	0.457	0.452	0.436	0.411	0.376	0.329	0.273	0.216	0.162	0.137
3.250	0.431	0.426	0.411	0.386	0.352	0.307	0.254	0.202	0.152	0.129
3.500	0.405	0.400	0.385	0.361	0.328	0.285	0.236	0.187	0.142	0.120
4.000	0.363	0.358	0.344	0.321	0.290	0.251	0.208	0.166	0.127	0.107
5.000	0.289	0.285	0.273	0.253	0.227	0.196	0.162	0.131	0.101	0.086
6.000	0.229	0.226	0.216	0.200	0.178	0.154	0.128	0.104	0.081	0.069

this formula (Appelbaum and Flood 1989*a, b*; Geels et al. 1989; Landis and Appelbaum 1990; Appelbaum and Flood 1990). Table IV is for an albedo of 0.1 and Table V is for an albedo of 0.4. A linear interpolation can extend the results to surfaces of arbitrary albedo.

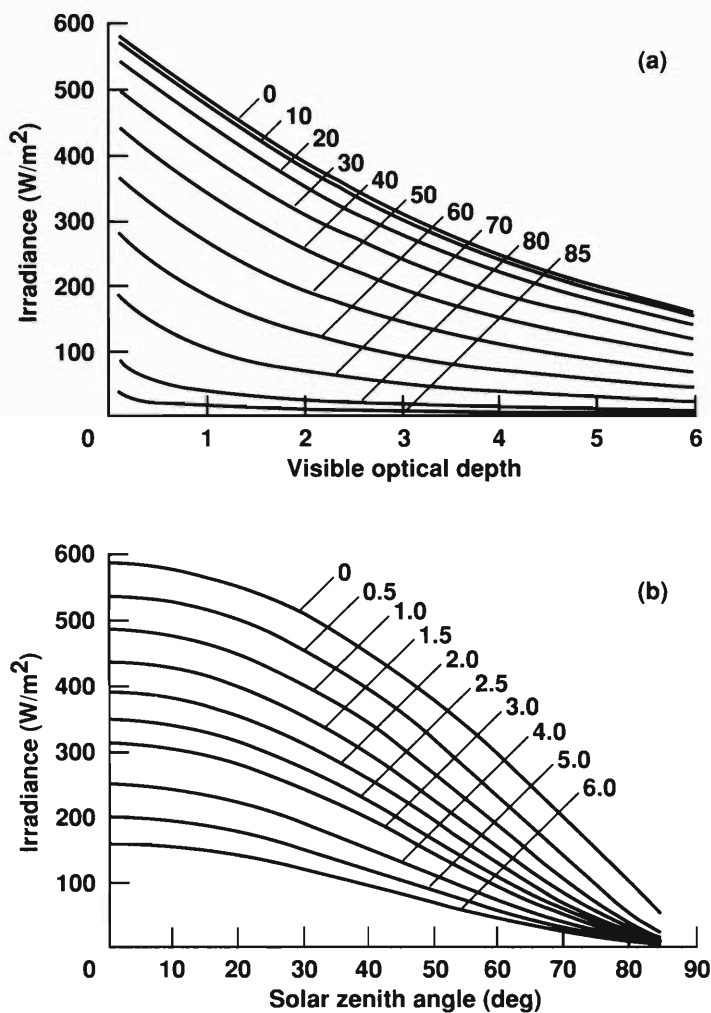


Figure 6. Top: Total irradiance (direct + diffuse) as a function of optical depth for 10 different zenith angles. The zenith angles correspond to those given in Tables IV and V. Bottom: Total irradiance as a function of zenith angle for 10 different optical depths. All irradiances are computed using the mean irradiance of 590 W m^{-2} at the top of the atmosphere.

Values of F_{tot} as a function of optical depth and zenith angle for $A = 0.25$ —typical for Mars—are shown in Fig. 6. It can be seen from this figure that substantial energy reaches the surface even at high optical depths. This is contrary to suggestions that dust storms would render solar-powered systems ineffective. At normal incidence, for example, almost 200 W m^{-2} are still

available at $\tau = 5$; even with the Sun only 30° above the horizon, 50 W m^{-2} are available. The reason for this is that Beer's law, which would reduce the energy by $e^{-5} = 0.007$ in this case, is not appropriate for a scattering atmosphere. Consequently, there is significant diffuse component of the radiation field that partially compensates for the reduction of the direct beam.

To illustrate this more quantitatively, the total downward irradiance can be separated into its direct, F_{dir} , and diffuse, F_{diff} , components. To make this separation using Pollack et al.'s data, subtract the direct irradiance

$$F_{\text{dir}} = S e^{-\frac{\tau}{\mu}} \quad (11)$$

from the total irradiance to obtain the diffuse irradiance, i.e.,

$$F_{\text{diff}} = S \left[\frac{f(\tau, \mu, A)}{(1 - A)} - e^{-\frac{\tau}{\mu}} \right]. \quad (12)$$

Note that F_{dir} and F_{diff} apply to a horizontal surface. As illustrated in Figs. 7 and 8, the direct component declines sharply and monotonically with increasing optical depth, while the diffuse component increases sharply, then falls off slowly with increasing optical depth. For both components, the incidence angle dependence is modest at normal incidence, and strong at grazing incidence. Thus, at large optical depths much of the direct beam is removed and converted into scattered radiation. It is this property of Martian dust that greatly enhances the viability of solar power on Mars. An example of how the direct, diffuse, and total radiation fields vary diurnally at the Viking Lander 1 site using the data of Pollack et al. is shown in Fig. 9. Again, the diffuse component dominates at high opacity, and is nontrivial at low opacity.

The total daily insolation on a horizontal surface and its direct and diffuse components can be calculated by integrating Eqs. (10)–(12) over the period from Sunrise to Sunset. The results are

$$\bar{F}_{\text{tot}} = \frac{S_0}{\pi} \left(\frac{\bar{r}}{r} \right)^2 \int_0^H \mu \frac{f(\tau, \mu, A)}{(1 - A)} dh \quad (13)$$

$$\bar{F}_{\text{dir}} = \frac{S_0}{\pi} \left(\frac{\bar{r}}{r} \right)^2 \int_0^H \mu e^{-\frac{\tau}{\mu}} dh \quad (14)$$

$$\bar{F}_{\text{diff}} = \frac{S_0}{\pi} \left(\frac{\bar{r}}{r} \right)^2 \int_0^H \mu \left[\frac{f(\tau, \mu, A)}{(1 - A)} - e^{-\frac{\tau}{\mu}} \right] dh. \quad (15)$$

Using the optical depth data from Fig. 1, Eqs. (13)–(15) can be used to determine the seasonal variation of the total daily irradiance at the Viking Lander sites. The results are shown in Fig. 10 along with the percentage of the total irradiance contributed by the diffuse component. During the spring and summer when the optical depth is relatively low, the diffuse component

TABLE V
 Normalized Net Irradiance Function for a Surface Albedo = 0.4

Optical Depth, τ	Solar Zenith Angle, Degrees									
	0	10	20	30	40	50	60	70	80	85
0.100	0.594	0.593	0.592	0.591	0.588	0.583	0.575	0.558	0.509	0.430
0.200	0.586	0.585	0.583	0.580	0.576	0.566	0.551	0.520	0.441	0.344
0.300	0.578	0.577	0.574	0.569	0.562	0.549	0.527	0.485	0.389	0.295
0.400	0.569	0.567	0.564	0.557	0.549	0.532	0.504	0.454	0.350	0.264
0.500	0.560	0.558	0.553	0.546	0.535	0.515	0.483	0.426	0.318	0.242
0.600	0.550	0.548	0.543	0.534	0.522	0.498	0.462	0.401	0.292	0.225
0.700	0.540	0.538	0.532	0.522	0.509	0.483	0.443	0.379	0.273	0.213
0.800	0.531	0.528	0.522	0.511	0.496	0.467	0.425	0.358	0.256	0.202
0.900	0.521	0.518	0.511	0.499	0.483	0.452	0.408	0.341	0.242	0.193
1.000	0.511	0.509	0.501	0.488	0.470	0.438	0.392	0.323	0.228	0.184
1.100	0.501	0.499	0.490	0.476	0.458	0.424	0.377	0.309	0.219	0.177
1.200	0.492	0.489	0.480	0.465	0.446	0.411	0.363	0.295	0.209	0.171
1.300	0.482	0.479	0.469	0.454	0.433	0.398	0.349	0.281	0.200	0.164

1.400	0.472	0.469	0.459	0.444	0.422	0.386	0.337	0.271	0.193	0.159
1.500	0.463	0.460	0.450	0.433	0.411	0.374	0.325	0.260	0.186	0.154
1.600	0.453	0.450	0.440	0.423	0.400	0.363	0.313	0.250	0.180	0.149
1.700	0.444	0.440	0.430	0.413	0.389	0.352	0.302	0.240	0.173	0.144
1.800	0.435	0.431	0.421	0.403	0.379	0.342	0.292	0.232	0.168	0.140
1.900	0.426	0.422	0.411	0.394	0.370	0.332	0.283	0.224	0.163	0.136
2.000	0.417	0.413	0.402	0.384	0.360	0.322	0.273	0.217	0.158	0.133
2.250	0.395	0.391	0.380	0.362	0.336	0.299	0.252	0.199	0.147	0.124
2.500	0.375	0.371	0.360	0.341	0.316	0.279	0.234	0.185	0.138	0.116
2.750	0.354	0.350	0.339	0.320	0.295	0.259	0.216	0.171	0.128	0.108
3.000	0.336	0.332	0.321	0.303	0.277	0.243	0.202	0.161	0.121	0.102
3.250	0.319	0.315	0.304	0.285	0.261	0.228	0.189	0.151	0.114	0.096
3.500	0.301	0.297	0.286	0.268	0.244	0.212	0.176	0.141	0.107	0.091
4.000	0.271	0.267	0.257	0.240	0.217	0.189	0.157	0.125	0.096	0.082
5.000	0.219	0.216	0.207	0.192	0.173	0.149	0.124	0.101	0.078	0.066
6.000	0.176	0.173	0.166	0.154	0.137	0.119	0.099	0.081	0.063	0.054

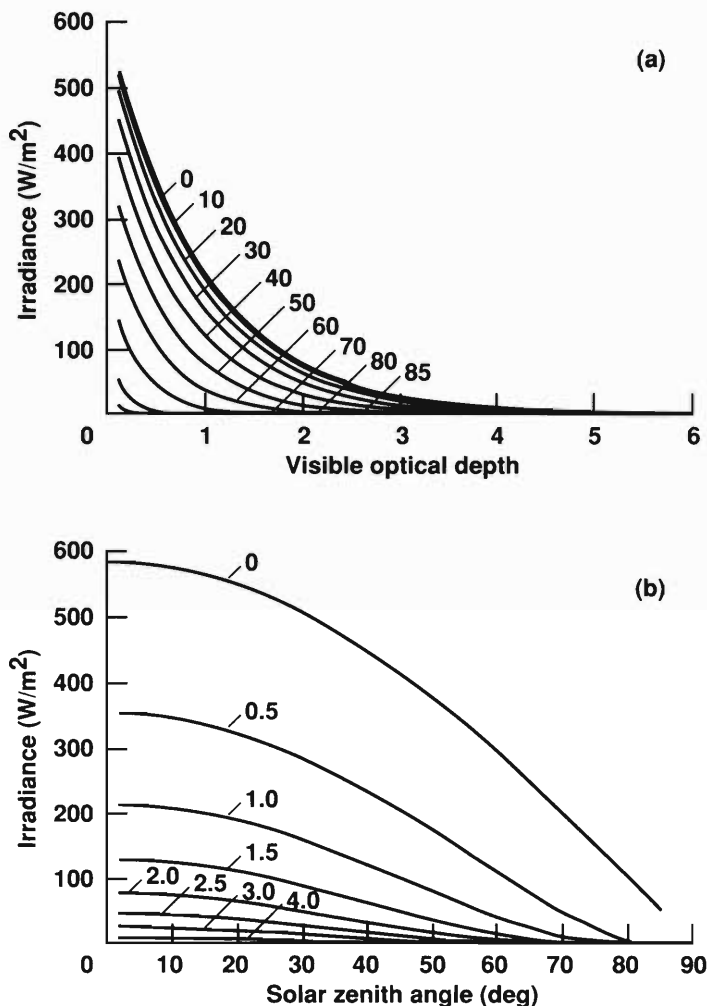


Figure 7. Same as in Fig. 6, but for the direct irradiance.

contributes almost half of the total irradiance at both sites; it rises to almost 90% during fall and winter when the optical depth is relatively high.

The advantage of using the data of Pollack et al. is that they are based on an accurate radiative transfer code. The disadvantage is that the dust optical properties are fixed. As discussed above, there are uncertainties in these properties and so it would be useful to know how well simpler transmission models compare with Pollack et al.'s in order to gain some flexibility in the calculations. For this purpose, two additional models have been chosen: a 2-stream model based on the Delta-Eddington approximation (Joseph et al. 1976), and a purely scattering model in which no absorption takes place at all ($\omega_o = 0$). As will be shown, the latter has a very simple analytical expression that is useful for quick estimates; it is also a much better representation of transmission than pure absorption (Beer's law).

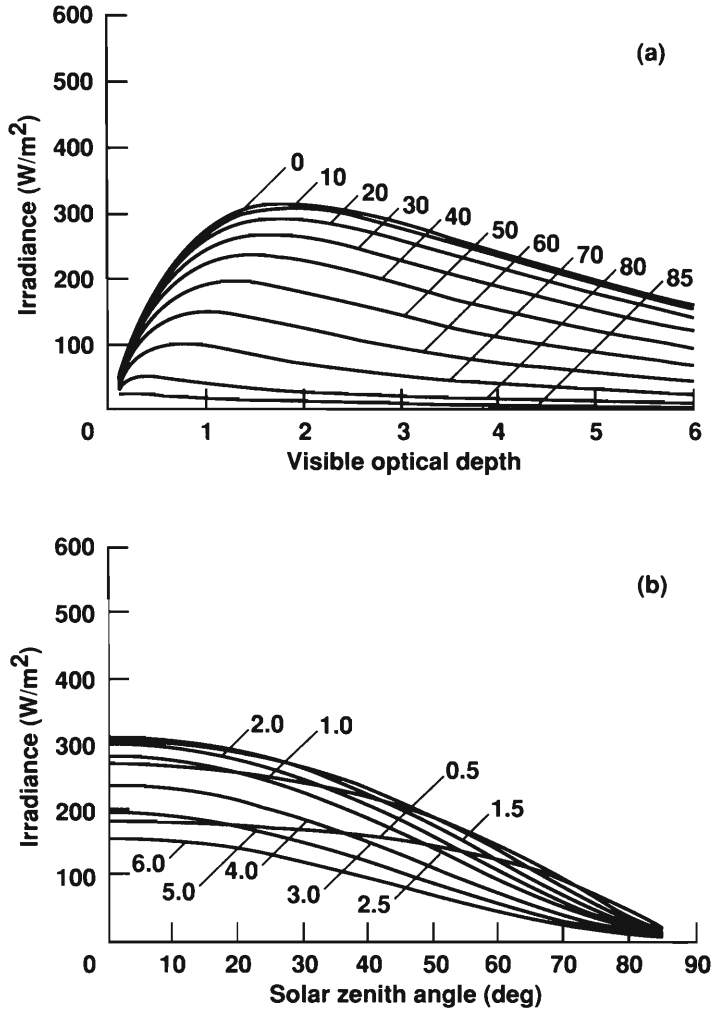


Figure 8. Same as in Fig. 6, but for the diffuse irradiance.

For a semi-infinite atmosphere overlying a reflecting (Lambertian) surface, the transmissivity (normalized by the μ -weighted incident irradiance) of solar radiation given by the Delta-Eddington approximation is

$$T(\mu, \tau, A) = c_1 e^{-k\tau} (1 + P) + c_2 e^{+k\tau} (1 - P) - (\alpha + \beta - 1) e^{-\frac{\tau}{\mu}} \quad (16)$$

where the constants c_1 and c_2 are

$$c_1 = - \frac{(1 - P) e^{-\frac{\tau}{\mu}} B - (\alpha + \beta) e^{+k\tau} C}{(1 + P) e^{+k\tau} C - (1 - P) e^{-k\tau} D} \quad (17)$$

and

$$c_2 = + \frac{(1 + P) e^{-\frac{\tau}{\mu}} B - (\alpha + \beta) e^{-k\tau} D}{(1 + P) e^{+k\tau} C - (1 - P) e^{-k\tau} D} \quad (18)$$

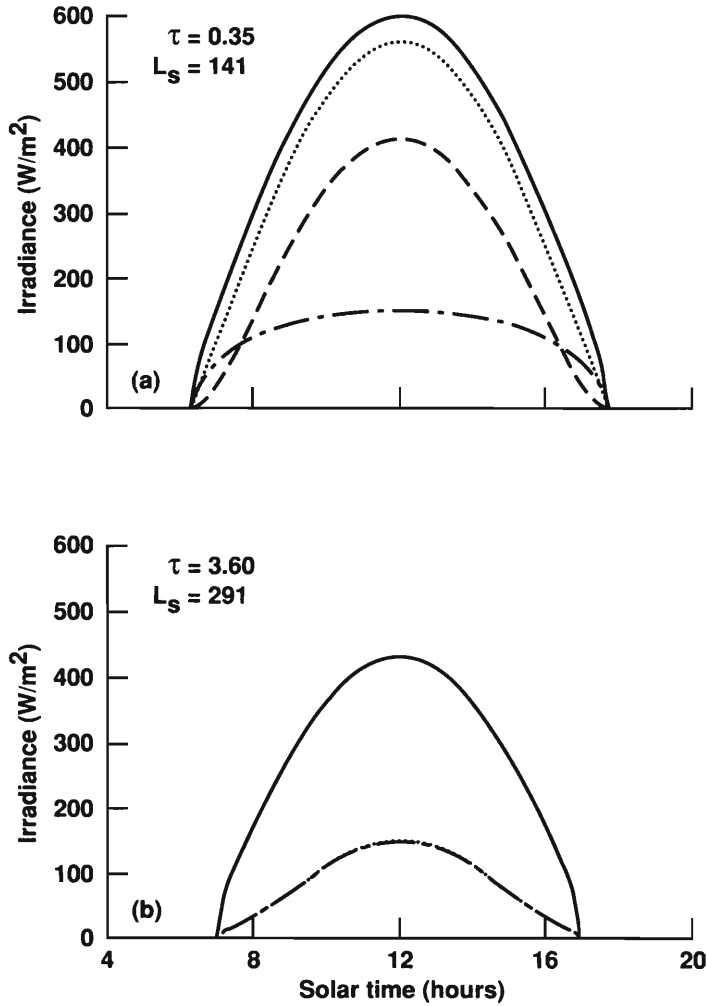


Figure 9. Diurnal variation of solar radiation at the Viking Lander 1 site for a midsummer season when the dust loading is minimal (top), and for an early winter season when it is large (bottom). The solid line represents the energy available to a horizontal collector at the top of the atmosphere; the dotted line represents the energy available at the surface and is therefore a measure of the extinction by dust. The dashed and solid-dotted curves show the direct and diffuse components, respectively. Virtually all of the radiation arriving at the surface in the winter case comes from the diffuse component.

where $B = A + (1 - A)\alpha - (1 + A)\beta$, $C = (1 - A) + P(1 + A)$ and $D = (1 - A) - P(1 + A)$.

$$k = [3(1 - \omega_0)(1 - g\omega_0)]^{\frac{1}{2}} \quad (19)$$

$$P = \frac{2}{3} \left[\frac{3(1 - \omega_0)}{(1 - g\omega_0)} \right]^{\frac{1}{2}} \quad (20)$$

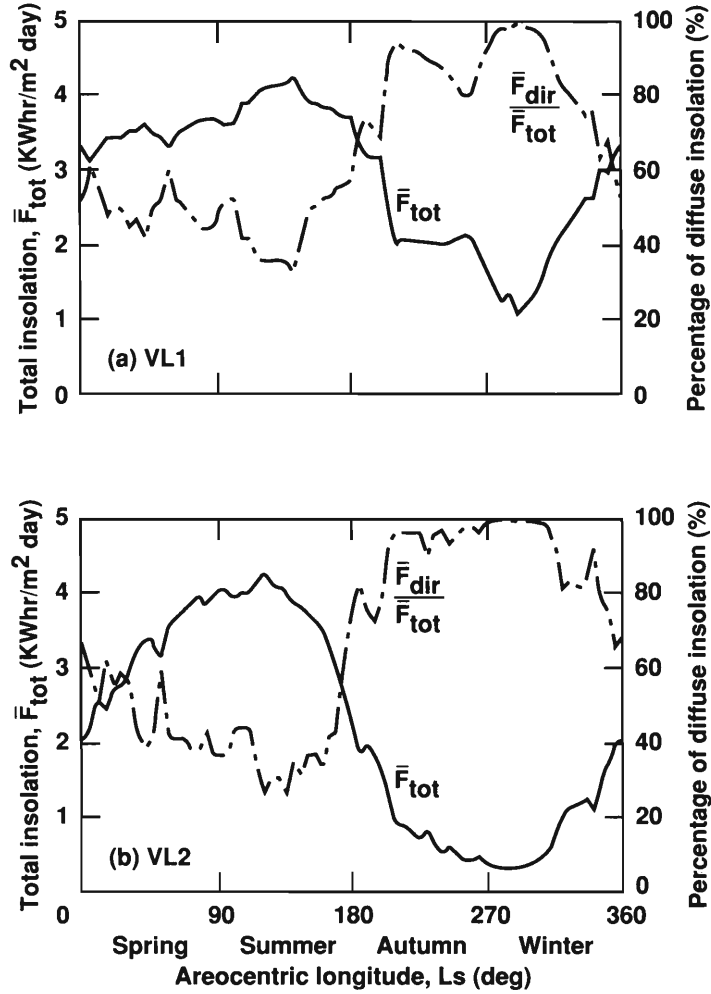


Figure 10. Seasonal variation of insolation at the two Viking Lander sites. Solid lines represent the daily-averaged total irradiance, dashed lines represent the percentage of that radiation due to the diffuse component.

$$\alpha = \frac{3}{4} \mu \omega_0 \left[\frac{1 + g(1 - \omega_0)}{1 - (\mu k)^2} \right] \quad (21)$$

$$\beta = \frac{1}{2} \mu \omega_0 \left[\frac{\left(\frac{1}{\mu} \right) + 3g\mu(1 - \omega_0)}{1 - (\mu k)^2} \right]. \quad (22)$$

A comparison of the Delta-Eddington and doubling code transmissivities is shown in Fig. 11. In general, the Delta-Eddington solution agrees well with the doubling code, but overestimates the transmissivity at low optical depths and underestimates it at high optical depths. These differences are mostly due to the multispectral nature of the doubling code calculations, as well as its accounting for the non-spherical shape of the dust particles. Also shown are

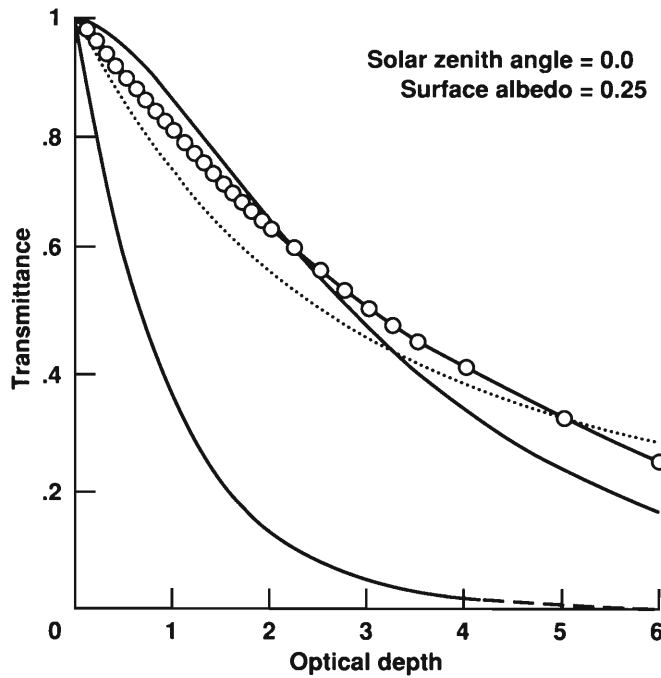


Figure 11. Dust transmissivities from several different radiation models. The solid curve with circles corresponds to the model of Pollack et al. (1990). The solid curve without circles is based on the Delta-Eddington 2-stream solution (Eq. 16). The dotted curve is based on a pure scattering model (Eq. 23), while the lower curve corresponds to Beer's law ($T = e^{-\tau/\mu}$).

the transmissivities for pure isotropic scatterers ($\omega_o = 1$) and pure absorbers ($\omega_o = 0$). The pure scattering transmissivity is

$$T(\mu, \tau) = \left(1 + \frac{\tau}{2\mu}\right)^{-1} \quad (23)$$

while that for pure absorption is simply $e^{-\tau/\mu}$ (Beer's law). In deriving Eq. (23) we have neglected reflection from the surface ($A = 0$). Clearly, the pure scattering approximation is much better than Beer's law.

The spectral dependence of the dust transmissivity is shown in Fig. 12. This dependence is calculated from Eq. (16) using the optical properties listed in Table III. In general, the spectral dependence is weak, but transmission does show a maximum near 800 nm. The sensitivity of existing photovoltaic cells has a similar frequency dependence, but with a response that is more sharply peaked and which maximizes at slightly longer wavelengths (900–1000 nm).

Clouds. A comparison of dust transmissivities with those for a postulated Martian water ice cloud ($\omega_o = 1$, $g = 0.6$) is shown in Fig. 13. Because of their higher single scattering albedos, clouds absorb less sunlight than dust particles and for any given optical depth, they transmit more sunlight to the surface. In designing solar-powered systems, therefore, a conservative

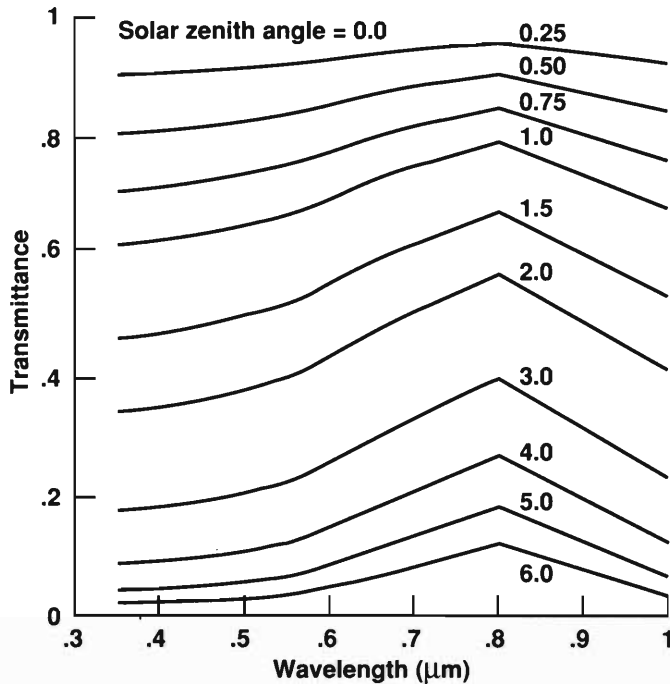


Figure 12. Spectral dependence of the dust transmissivity at visible wavelengths for several different optical depths. Transmissivities are calculated from Eq. (16).

approach would be to assume that dust rather than clouds will be the principal agent of extinction.

IV. POINTING TRADEOFFS

Because of atmospheric scattering by dust particles, tracking the direct beam may not always be the optimum collection strategy. Even with modest amounts of dust in the atmosphere, the diffuse component can be substantial. For Martian dust, the daily integrated diffuse irradiance falling on a horizontal collector becomes comparable to the direct beam irradiance well before the optical depth reaches unity (Fig. 14). At the equator, the two components are comparable at optical depths of 0.6 to 0.8. However, at high latitudes the longer slant path and higher zenith angle lowers the value to between 0.2 and 0.3. As a solar-pointed collection system will lose some fraction of the diffuse component (it will not be able to see the full 2π steradians of the sky), there will be a "breakpoint" at which it is no longer advantageous to point the collectors.

In this section, the performance characteristics of four pointing systems of two general classes are discussed: stationary (horizontal and equator/meridian) and tracking (one-axis Sun-tracking and two-axis Sun-tracking). Stationary systems have the advantage of simplicity, but cannot realize the full potential of the direct beam. Tracking systems make up for this disadvan-

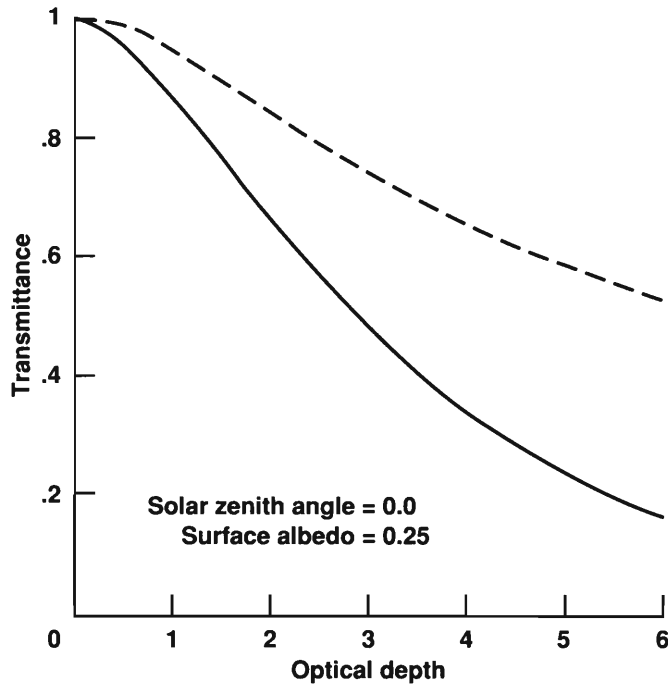


Figure 13. Dust (solid line) and water-ice cloud (dashed line) transmissivities for a single value of the zenith angle (0°). Transmissivities are calculated from Eq. (16).

tage, but not without complexity (power supplies, control systems, tracking electronics, etc.). The engineering tradeoffs between mass, complexity, reliability, etc., will depend on the particular application and are beyond the scope of this chapter.

A. Generalized Design Equations for Tilted Collectors

The equations for the total daily irradiance falling on horizontal collectors have already been presented (Eqs. 13–15). In this subsection a generalized set of design equations for tilted collectors is presented. The equations are expressed in terms of α , the angle the collector is tilted with respect to the horizontal, and α_s the angle between the collector normal and Sun direction.

In clear sky conditions (no dust in the atmosphere), the daily averaged surface insolation is simply

$$\bar{F}_{\text{tot}} = \frac{S_0}{\pi} \left(\frac{\bar{r}}{r} \right)^2 \int_0^H \cos(\alpha_s) dh \quad (24)$$

In dusty conditions, however, tilted collectors will receive an additional contribution due to reflection from the ground such that the instantaneous total irradiance is

$$F_{\text{tot}} = F_{\text{dir}} + F_{\text{diff}} + F_{\text{gnd}} \quad (25)$$

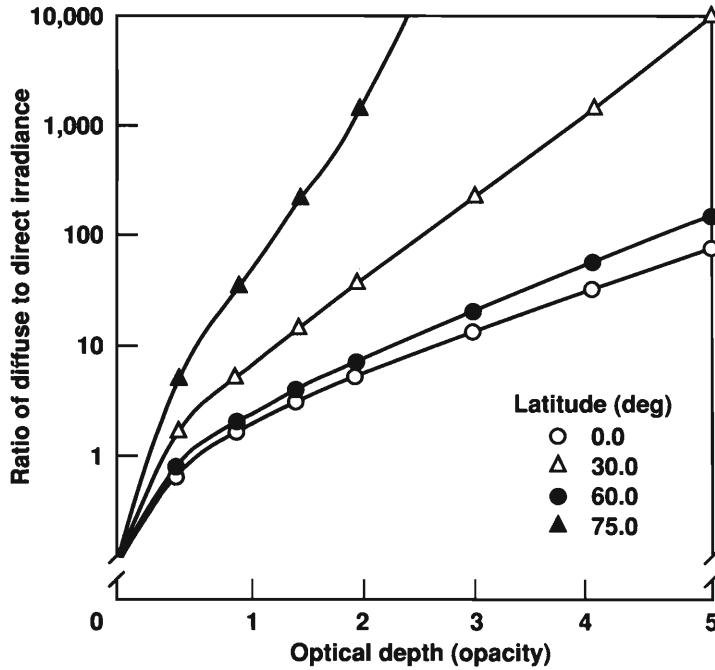


Figure 14. Ratio of the daily integrated diffuse/direct irradiance as a function of optical depth for several different latitudes at northern spring equinox.

where the direct irradiance is

$$F_{\text{dir}} = S_0 \left(\frac{\bar{r}}{r} \right)^2 \cos(\alpha_s) e^{-\frac{\tau}{\mu}} \quad (26)$$

and the diffuse irradiance is

$$F_{\text{diff}} = \mu S_0 \left(\frac{\bar{r}}{r} \right)^2 \left[\frac{f(\tau, \mu, A)}{(1-A)} - e^{-\frac{\tau}{\mu}} \right] \cos^2 \left(\frac{\alpha}{2} \right). \quad (27)$$

The reduced sky coverage of a tilted collector is represented by the $\cos^2(\alpha/2)$ term in Eq. (27). This term arises by weighting the contribution from each strip of sky at angle β with respect to the collector axis by $\cos(\beta)$, and integrating over the $2(\pi - \alpha)$ steradians viewable by the collector. It is also worth noting that Eq. (26) contains an implicit dependence of the solar zenith angle through Beer's law.

The irradiance due to ground reflection depends on the surface albedo A and the total (direct+diffuse) irradiance incident on the ground. The ground reflection contribution to collector irradiance is

$$F_{\text{gnd}} = A \mu S_0 \left(\frac{\bar{r}}{r} \right)^2 \frac{f(\tau, \mu, A)}{1-A} \sin^2 \left(\frac{\alpha}{2} \right) \quad (28)$$

where $\sin^2(\alpha/2)$ represents the effect of projecting the ground irradiance onto the collector.

The daily-averaged surface insolation for dusty conditions is therefore

$$\bar{F}_{\text{tot}} = \frac{1}{\pi} \int_0^H (F_{\text{dir}} + F_{\text{diff}} + F_{\text{gnd}}) dh. \quad (29)$$

B. Equator/Meridian System

The Equator/Meridian (E/M) system is pointed toward the intersection of the local meridian and the equator and is inclined to the horizon at an angle equal to its latitude. At the equinoxes, therefore, the E/M system receives the full direct beam at local noon. At other seasons, the angle between the collector normal and Sun direction at noon is equal to the solar declination, i.e., $\alpha_s = \delta$. E/M systems have an advantage over horizontal systems in that the daily averaged collector/Sun angle is lower at latitudes away from the equator. However, this advantage is offset by the loss in diffuse irradiance due the limited view of the sky afforded E/M systems, particularly at high latitudes. In addition, the E/M system does not perform well during spring and summer when the Sun is higher in the sky. For the E/M system

$$\alpha = \theta \quad (30)$$

$$\cos(\alpha_s) = \cos(\delta) \cos(h). \quad (31)$$

For clear sky conditions, the daily averaged irradiance is

$$\bar{F}_{\text{tot}} = \frac{S_0}{\pi} \left(\frac{\bar{r}}{r} \right)^2 \int_0^H \cos(\delta) \cos(h) dh = \frac{S_0}{\pi} \left(\frac{\bar{r}}{r} \right)^2 \cos(\delta) \sin(H), H < \frac{\pi}{2} \quad (32)$$

or

$$= \frac{S_0}{\pi} \left(\frac{\bar{r}}{r} \right)^2 \int_0^{\frac{\pi}{2}} \cos(\delta) \cos(h) dh = \frac{S_0}{\pi} \left(\frac{\bar{r}}{r} \right)^2 \cos(\delta), H \geq \frac{\pi}{2}. \quad (33)$$

C. One-Axis Sun Tracking System

The one-axis system consists of a single drive on a polar mount rotating at an angular velocity equal to the rotation of the planet, but in the opposite direction. This enables the collector to track the diurnal motion of the Sun's projection on the equator. However, seasonal changes in the solar declination cannot be followed with one-axis systems. Thus, the maximum collector/Sun angle will be equal to the planet's obliquity. For the one-axis system,

$$\cos(\alpha) = \cos(\theta) \cos(h) \quad (34)$$

$$\alpha_s = \delta. \quad (35)$$

For clear sky conditions, the daily averaged surface insolation is

$$\overline{F}_{\text{tot}} = \frac{S_0}{\pi} \left(\frac{\bar{r}}{r} \right)^2 \int_0^H \cos(\delta) dh = \frac{S_0}{\pi} \left(\frac{\bar{r}}{r} \right)^2 \cos(\delta) H. \quad (36)$$

D. Two-Axis Sun Tracking Systems

Two-axis systems simultaneously follow the diurnal and seasonal motion of the Sun. In this case, $\alpha_s = 0$ and the tilt angle is the same as the solar zenith angle,

$$\cos(\alpha) = \sin(\theta) \sin(\delta) + \cos(\theta) \cos(\delta) \cos(h). \quad (37)$$

For clear sky conditions, the daily averaged surface insolation is

$$\overline{F}_{\text{tot}} = \frac{S_0}{\pi} \left(\frac{\bar{r}}{r} \right)^2 \int_0^H dh = \frac{S_0}{\pi} \left(\frac{\bar{r}}{r} \right)^2 H. \quad (38)$$

E. Results

The daily averaged surface insolation (including the diffuse and ground reflected components) as a function of season, dust opacity, and latitude for each of the four different pointing systems is shown in Figs. 15–19. In general, tracking systems outperform stationary systems when the opacity is low ($\tau < 0.2$). While this is true for all latitudes and seasons, the break-even point does have a latitudinal dependence. At high latitudes, for example, the Sun is never very high on the horizon and a tracking system (one- or two-axis) will annually gather about five times the energy of a horizontal collector. At the equator, on the other hand, Sun-trackers boost the annual gain by only 50% over a horizontal system. Thus, high latitude operations clearly favor a tracking system—if atmospheric scattering is negligible.

However as the optical depth increases, tracking systems lose their advantage and horizontal systems yield better performance. Importantly, this changeover occurs at optical depths that frequently occur on Mars ($\tau \leq 1$). At the poles, the longer slant path (increased scattering) and higher zenith angles (reduced direct irradiance) result in a lower break-even optical depth ($\tau \sim 0.7$) than at lower latitudes ($\tau \sim 1.0$). For all latitudes and seasons, however, horizontal systems are superior to tracking systems when the optical depth exceeds unity.

V. ENVIRONMENTAL CONCERNS

Aside from the availability of sunlight, photovoltaic performance on Mars will also depend on temperature, wind, dust accumulation and abrasion. The annual mean surface temperature of the planet is ~ 215 K. However, surface temperatures can vary from as low as 130 K in the winter polar regions, to as high as 300 K in the southern hemisphere subtropics (Kieffer et al. 1977). The

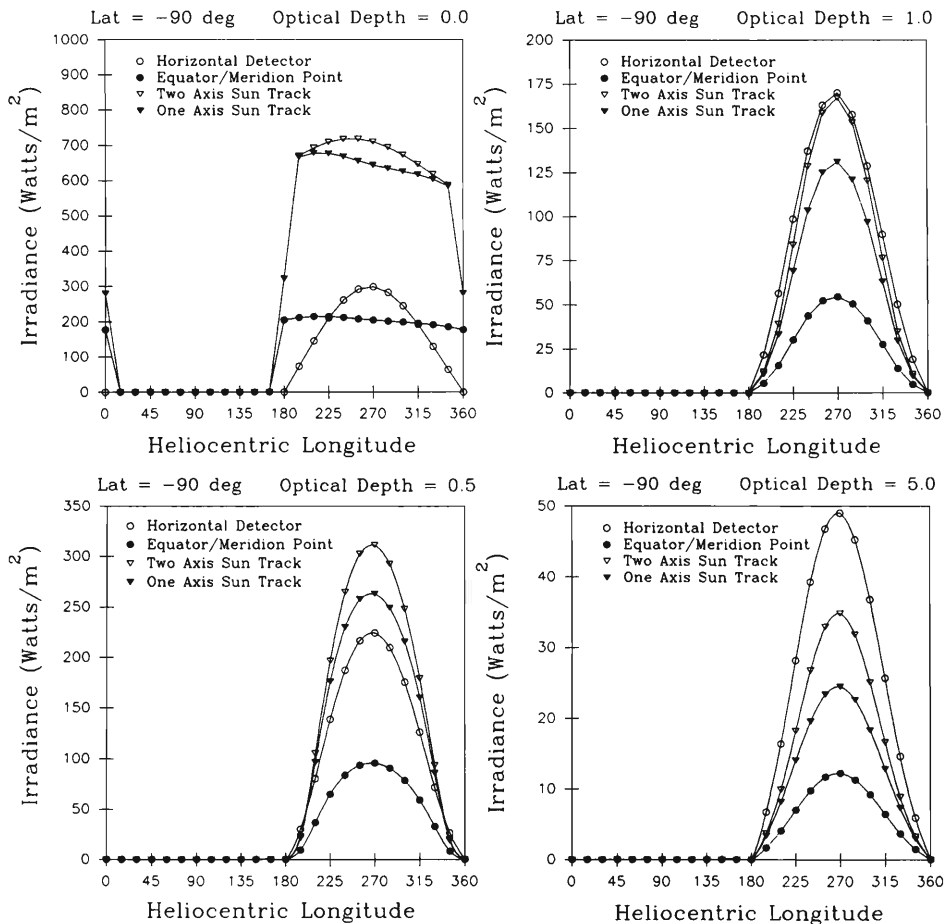


Figure 15. The daily averaged insolation collected by the different pointing systems at the south pole as a function of season and optical depth. The different systems are: horizontal detector (open circles), Equator/Meridion Pointing (filled circles), two-axis Sun tracker (open triangles), one-axis Sun tracker (filled triangles).

latter occurs at noon when the planet is close to perihelion ($L_s = 250^\circ$); at night in these regions, the surface cools to about 180 K. Thus, the diurnal range of Martian surface temperatures can also be quite large. In general, solar cells perform better in low temperatures with peak performance occurring between 150 and 200 K; at lower temperatures their efficiency declines.

Solar arrays on Mars will have to withstand wind loads. Winds have been measured at the Viking Lander sites at a height of 1.6 m above the surface (Hess et al. 1977). Like temperature, they exhibit significant diurnal and seasonal variability. During summer, the strongest winds occurred at midday: about 6 to 7 m s⁻¹ at Viking Lander 1 site, and about 3 to 4 m s⁻¹ at Viking Lander 2 site. During winter, stronger mean winds developed with occasional gusts in excess of 25 m s⁻¹ at Viking Lander 1 and 15 m s⁻¹ at Viking Lander 2. Winds of this magnitude were relatively infrequent, and

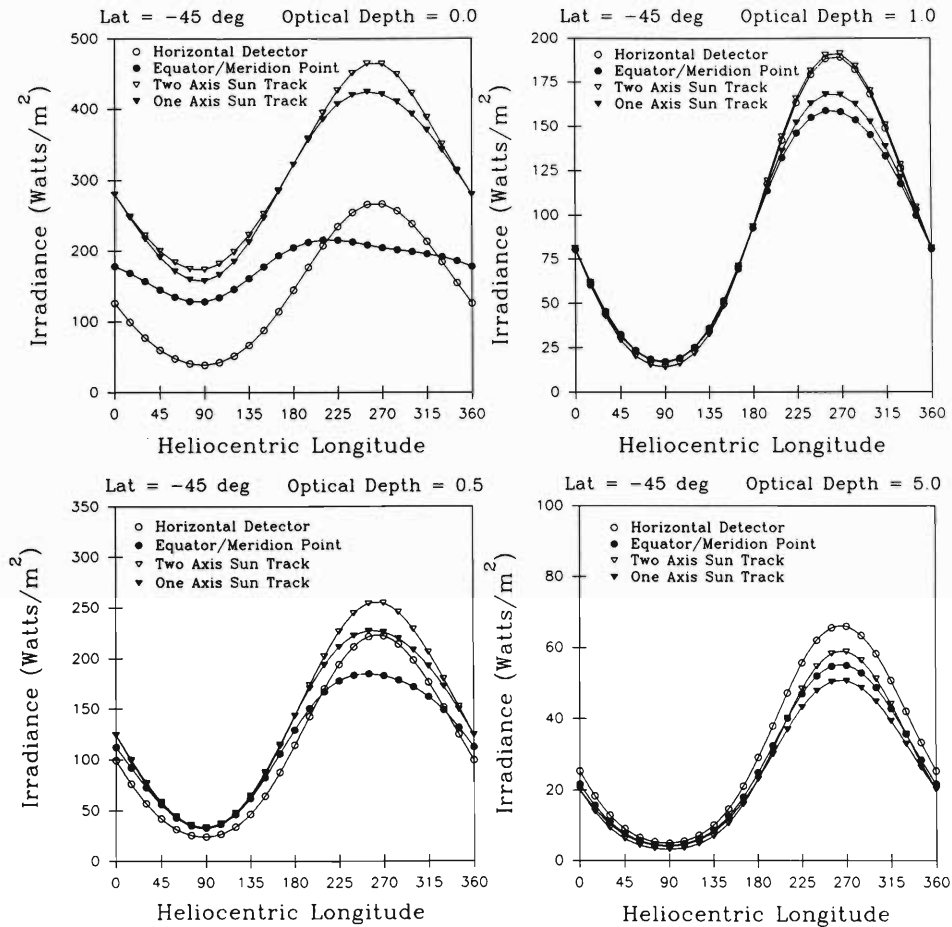


Figure 16. Same as Fig. 15, but for 45°S latitude.

occurred less than 0.01% of the time. The dynamic pressures associated with these winds are 5 to 10 Nt m⁻².

Dust accumulation is a potentially significant problem for solar power. During a great dust storm the atmosphere suspends as much as 10 μm of dust (see Sec. II). If the mean particle size is several μm , then 10 μm of dust represents several monolayers of potential accumulation. The performance of solar cells would be seriously degraded if covered by several monolayers of dust. Thus, occasional cleaning is required. Recent wind tunnel tests show that this might be accomplished by tilting the arrays into the wind (Gaier et al. 1990). The most efficient cleansing occurred for tilt angles of 45°, though the angular dependence was not particularly sharp. However, cleansing was minimal for all angles at wind speeds $<30 \text{ m s}^{-1}$. As surface winds of this magnitude are relatively infrequent, a more direct method for cleansing solar arrays is required.

Abrasion is also a potentially significant problem. Abrasion by wind-blown dust of the approximate elemental composition and size as found on

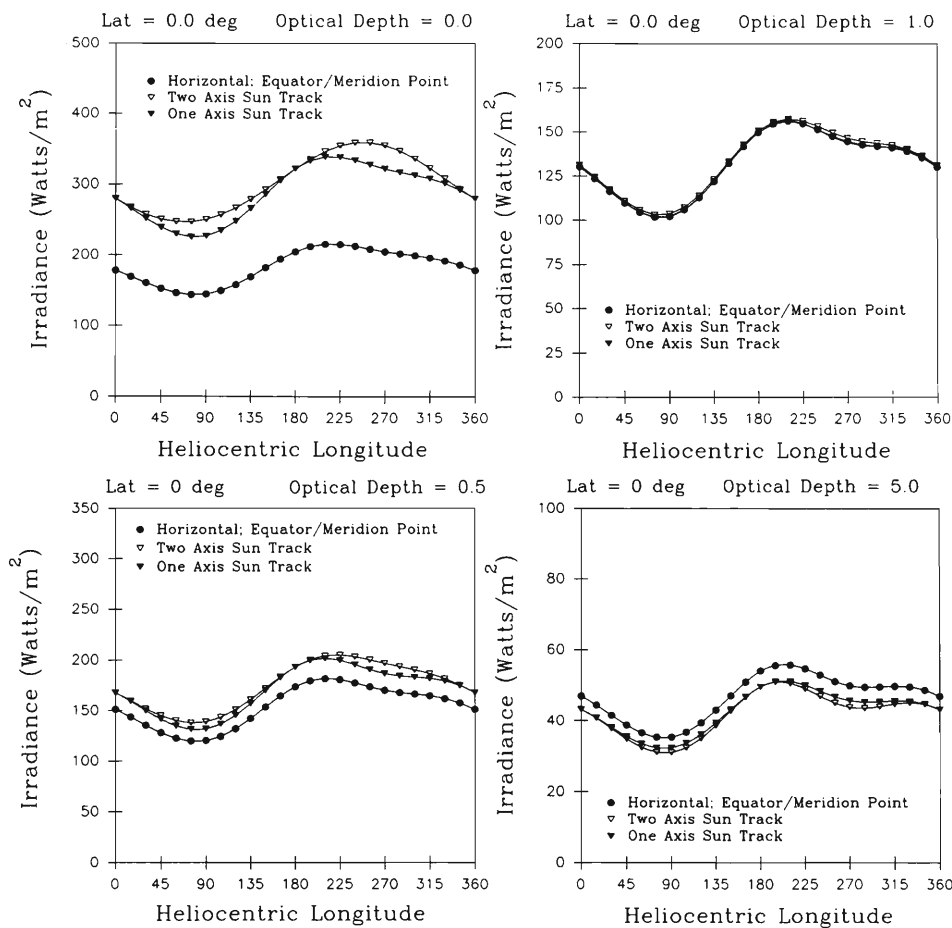


Figure 17. Same as Fig. 15, but for the equator.

Mars has been measured for typical solar cell coverglass (Gaier and Perez-Davis 1992). The results suggest that performance degradation is a concern only for very large wind speeds (85 m s^{-1}), and only for vertically oriented arrays. Worst-case abrasive losses were at the several percent level and did not seriously degrade power production. To some extent, this finding is corroborated by the relative lack of abrasion damage on the Viking Lander optical elements. Thus, as long as the arrays are glass-coated, abrasion may not be a significant problem.

However, as an additional precaution against abrasion it would be desirable to position the arrays above the saltation height. Saltation is the process believed to be responsible for lifting dust particles into the Martian atmosphere (Greeley and Iverson 1985). Winds first set into motion sand-sized particles ($\sim 100 \mu\text{m}$ in diameter) which follow modified ballistic trajectories and fall back to the surface. Upon impacting the surface, they suspend the smaller dust-sized particles which are carried to great heights. For Mars, sand-sized particles will “saltate” to about 20 cm above the surface. Positioning solar

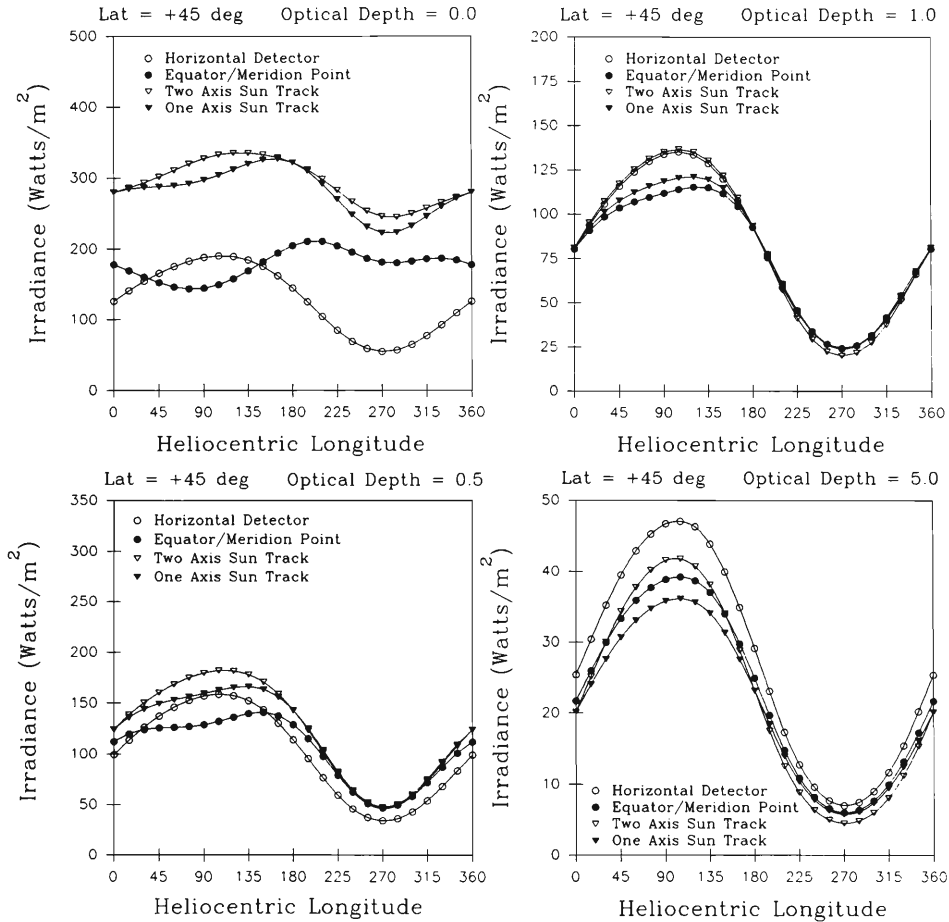


Figure 18. Same as Fig. 15, but for 45°N latitude.

arrays above this height will further reduce the risk of abrasion by wind-blown sand.

VI. APPLICATION TO SURFACE SYSTEMS

The previous sections have laid out a procedure for calculating the amount of solar radiation reaching the surface of Mars at any given latitude, season, dust loading, and pointing configuration. In this section, the state-of-the-art in photovoltaic power system technology is briefly reviewed, and the power requirements of a hypothetical mission and a resource application are analyzed.

A. Solar Cell Technology

There are three approaches to photovoltaic power: conventional flat-plate arrays, thin-film solar cells, and concentrator systems. A discussion of these

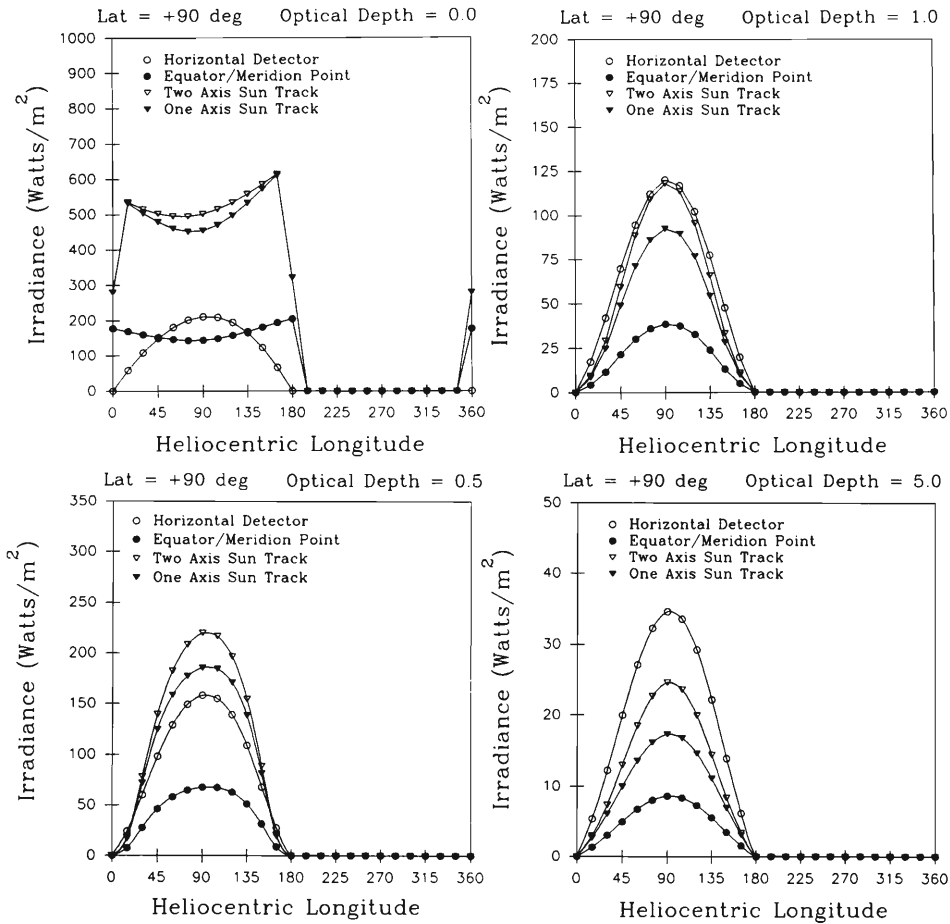


Figure 19. Same as Fig. 15, but for the north pole.

approaches can be found in Green (1982), Buresch (1983), Van Overstraaten and Mertes (1986), and Landis and Appelbaum (1991).

Conventional arrays for space flight use either crystalline silicon (Si) or gallium arsenide (GaAs) solar cells. The Si arrays have been used the most and are well developed. Their characteristics are well known and they have demonstrated conversion efficiencies of ~14% in space. Some Si cells have up to 20% conversion efficiencies, but these have not yet been flight qualified. GaAs cells are smaller and more efficient than Si cells, but are heavier and more brittle. The GaAs cells currently on the market have an average conversion efficiency of 18.5%, although higher efficiencies (21.5%) have been achieved in the laboratory. Several technologies are under development to make GaAs cells lighter. The most advanced of these is CLEFT, where a thin (5 μm) large-area cell has been separated from a single-crystal substrate (Fan et al. 1981).

Of importance to power system analysis is the specific power (power output per unit mass). At present, the specific power of Si arrays has been

demonstrated on the Solar Array Flight Experiment (SAFE) aboard the Space Shuttle at 66 W kg^{-1} . A recent design, but not yet flown, achieved 130 W kg^{-1} . This design, from the Advanced Photovoltaic Solar Array (APSA) program, is based on 2 mil thick Si cells. The long-term goals are to combine the APSA and CLEFT technologies to develop specific powers of 300 W kg^{-1} . All of these designs are intended for the zero gravity conditions of low Earth orbit and must be scaled for application to Mars. Furthermore, these figures measure the specific power at the array level which includes the cell, blanket, and array structure masses. Currently, the array structure and its power management and distribution system account for almost three-quarters of the total power system mass. Clearly, there is powerful incentive to reduce the masses of these components.

Thin-film solar cell technology is relatively recent and is not yet flight qualified. In this approach, the arrays are constructed from thin layers ($1\text{--}5 \mu\text{m}$) of highly absorbing photovoltaic materials that are deposited onto a flexible substrate. Three materials have been used: amorphous silicon ($\alpha\text{-Si}$), copper indium diselenide (CuInSe_2), and cadmium telluride (CdTe). The advantage of thin-film cells is their potential for high specific power ($1\text{--}15 \text{ kW kg}^{-1}$) in spite of their low inherent conversion efficiencies ($5\text{--}10\%$). Unfortunately, the development of this technology has been driven by surface-based applications on Earth. Consequently, very little research into developing lightweight systems for space applications has been carried out. Improvements in conversion efficiency and cell performance degradation will greatly benefit this approach.

Concentrator systems focus light onto small, extremely high-efficiency solar cells. This approach has been tested in space only on small-scale experiments. Although conversion efficiencies over 30% have been demonstrated, concentrator systems have inherent limitations for surface power on Mars because they focus the direct beam only. If a power system must be designed to operate under worst-case conditions, then concentrator systems can be ruled out.

Many resource processing technologies require thermal processing. One method of achieving high temperatures is the “solar furnace” using concentrating mirrors or lenses. Because a solar furnace, like a concentrator PV system, only utilizes the direct beam component of solar radiation, the low direct beam insolation on Mars makes the utility of this approach much lower than in other environments.

B. Energy Storage

For human outposts, continuous power will be required. Because Mars is subject to a 12 hr night and prolonged dust storms, some of the energy collected during the day must be stored. The amount of storage will depend on location and season. As the base location is moved away from the equator, the night length decreases during summer and increases during winter. The

night length in Earth hours is

$$T_n = 24 - T_d \quad (39)$$

where

$$T_d = 0.1369 \cos^{-1}(-\tan \theta \tan \delta) \quad (40)$$

is the number of daylight hours.

Conventional storage systems are likely to be inadequate for human outposts (McKissock et al. 1990). Their capacities range from 10 W-hr kg⁻¹ for nickel-cadmium batteries operating at 25% depth of discharge (Halpert 1985), to about 80 W-hr kg⁻¹ for lithium/SO₂ batteries operating at 40% depth of discharge (Linden 1984). To deliver a 25 kW hr⁻¹ load would require battery masses of the order of 300 to 2500 kg. A better candidate is the hydrogen-oxygen cell (RFC) with either pressurized gas or cryogenic liquid storage. RFC energy storage densities have been shown to approach 1000 W-hr kg⁻¹ (Martin et al. 1985).

C. Sample Case: PV Power System for a Hypothetical Human Outpost

The primary use of the solar radiation data presented here is to permit a more accurate assessment of photovoltaic power-system sizes and masses for system analysis and tradeoff studies. An example of such an analysis is given in Table VI for a human outpost located at the Viking Lander 1 site with a crew size of 15, and a power demand of 25 kWe during the day and 12.5 kWe at night. The analysis is carried out for two different solar cell options (α -Si and GaAs), and two different energy storage options (Li-SO₂ batteries and hydrogen-oxygen RFCs). The cell efficiencies of both types are near their optimum values. Both cell types are assumed to be integrated into a suitable lightweight flexible blanket assembly with a specific mass of 0.5 kg m⁻² for the GaAs cell, and 0.04 kg m⁻² for the α -Si cell. Added to these is the array structure specific mass which is 0.56 kg m⁻² for each type. The storage system efficiency takes into account the storage "round-trip" efficiency as well as the power management and distribution efficiencies. For Li/SO₂ batteries, the round trip efficiency is 0.9 and 40% depth of discharge. For each system, the array is assumed to be fixed in the horizontal plane with no pointing capability as might be the case if operational simplicity is desired for deployment. For a relatively short mission—one that arrives and departs during midsummer ($L_s = 141^\circ$)—Table VI indicates that at least 660 m² of solar panels and 845 kg of total mass (panels + energy storage) are required.

D. Sample Case: PV Power System for the "Mars Direct" Scenario

In-situ propellant generation on Mars is an option for drastically reducing the cost of Mars expeditions. Baker and Zubrin (1990) and Zubrin et al. (1991) have proposed that 107 tons of methane/oxygen propellant can be produced on Mars from 5.7 tons of hydrogen brought from Earth plus CO₂ from the

TABLE VI
Mars Mission Power System Comparison
Performance at $L_s = 141, 22^\circ 3 \text{ N}, \tau = 0.35$

Day length:		13.18 hr						
Night length:		11.47 hr						
Average Daytime Insolation:		305 W m ⁻²						
Energy Storage Requirement:		143 kW-hr						
System	Cell Efficiency	Array Size (m ²)	Array sp. Mass (kg m ⁻²)	Array Mass (kg)	Storage Capacity (W-hr/kg)	Storage Mass (kg)	System Mass (kg)	
	α -Si/Li-SO ₂	0.12	1210	0.6	726	200	1790	2516
	GaAs/Li-SO ₂	0.22	660	1.06	700	200	1790	2490
	α -Si/RFC	0.12	1210	0.6	726	1000	145	871
	GaAs/RFC	0.22	660	1.06	700	1000	145	845

Martian atmosphere. They estimate that the energy requirements for this scenario could be met with a 100 kW reactor running continuously (day and night) for 155 days. This is equivalent to 370 MW-hr of electrical energy.

To determine if these requirements can be met with a surface photovoltaic array, the following assumptions are made:

1. The production plant is located at the Viking Lander 1 site.
2. Production is completed during spring and summer.
3. The production process stops at night.
4. The arrays are fixed and horizontal (no tracking).
5. Solar array specific mass = 0.9 kg m^{-2} (APSA technology).
6. Solar array efficiency = 20% at Mars (GaAs technology).
7. No mass allocation for energy storage.

The global insolation on a horizontal surface at Viking Lander 1 averages slightly more than 3 kW-hr m^{-2} per day during spring and summer. This period is chosen because of its relatively low atmospheric dust content. Running the system for this time (half a Mars year) gives a total insolation of about $1000 \text{ kW-hr m}^{-2}$. Thus, the arrays will produce about 200 kW-hr m^{-2} of electrical energy, and the required array area and mass is 1850 m^2 and 1.67 metric ton. This is comparable to the baseline power system of the 100 kW nuclear reactor at 3.96 metric tons considered in the Zubrin/Baker architecture.

VII. CONCLUSION

The utilization of solar energy as a power source for surface-based operations on Mars depends on the attenuating effects of its atmosphere as well as the location and season of interest. In this chapter, we have summarized what is known about the Martian atmosphere as it relates to solar power, and have presented a procedure for calculating the amount of solar radiation available at the surface as a function of latitude, season, time of day, and atmospheric dust load (optical depth).

A major concern for solar power on Mars has been the dust storms which can occur on local to global scales, and which can last for several months. The concern is not only for their effect on array output, but also for their potential to cover and/or abrade the arrays themselves. The former appears to be more of an issue and may require some kind of cleansing device. The latter is less of an issue as long as the arrays have a glass overcoat. However, as far as the attenuating effect of suspended dust particles is concerned, solar power remains a viable energy source on Mars. As has been pointed out by others, dust particles suspended in the Martian atmosphere scatter as well as absorb, and it is this property that allows enough sunlight to reach the surface to justify photovoltaic systems.

Acknowledgments. This work was supported by the Planetary Atmospheres Program of the National Aeronautics and Space Administration and was

performed in part at NASA's Ames and Lewis Research Centers.

REFERENCES

- Appelbaum, J., and Flood, D. 1989a. *Photovoltaic Power System Operation in the Mars Environment*, NASA TM-102075.
- Appelbaum, J., and Flood, D. 1989b. Solar radiation on Mars. *Solar Energy* 45:353–363, and NASA TM-102299.
- Appelbaum, J., and Flood, D. 1990. *Solar Radiation on Mars—Update 1990*, NASA TM-103623.
- Arvidson, R. E., Guinness, E. A., Moore, H. J., Tillman, J. E., and Wall, S. D. 1983. Three Mars years: Viking Lander 1 imaging observations. *Science* 222:463–468.
- Baker, D., and Zubrin, R. M. 1990. Mars direct: Combining near-term technologies to achieve a two-launch manned Mars mission. *J. British Interplanet. Soc.* 43:519–523.
- Banks, P. M., and Kockarts, G. T. 1973. *Aeronomy Part A* (New York: Academic Press).
- Barth, C. A. 1985. Photochemistry of the atmosphere of Mars. In *The Photochemistry of Atmospheres, Earth, the Other Planets, and Comets*, ed. J. Levine (Orlando, FL: Academic Press).
- Briggs, G. A., and Leovy, C. B. 1974. Mariner 9 observations of the Mars north polar hood. *Bull. Amer. Meteorol. Soc.* 55:278–296.
- Buresch, M. 1983. *Photovoltaic Energy Systems: Design and Installation* (New York: McGraw-Hill).
- Clancy, R. T., and Lee, S. W. 1991. A new look at dust clouds in the Mars atmosphere: Analysis of emission-phase-function sequences from global Viking IRTM observations. *Icarus* 93:135–158.
- Clark, B. C., Baird, A. K., Weldon, R. J., Tsusaki, D. M., Schnabel, L., and Candelaria, M. P. 1982. Chemical composition of Martian fines. *J. Geophys. Res.* 87:10059–10067.
- Colburn, D., Pollack, J. B., and Haberle, R. M. 1989. Diurnal variations in optical depth at Mars. *Icarus* 79:159–189.
- Curran, R. J., Conrath, B. J., Hanel, R. A., Kunde, V. G., and Pearl, J. C. 1973. Mars: Mariner 9 spectroscopic evidence for H₂O clouds. *Science* 182:381–383.
- Daumont, D., Brion, J., and Malicet, J. 1983. Measurement of total atmospheric ozone: Consequences entailed by new values of ozone absorption cross-sections at 223K in the 310–350 nm spectral range. *Planet. Space Sci.* 31:1229–1234.
- Fan, J. C. C., Bozler, C. O., and McClelland, R. W. 1981. Thin film Ga-As solar cells. In *Proc. of 15th IEEE Photovoltaic Specialists Conf.* (New York: Inst. of Electrical and Electronic Engineers), pp. 666–672.
- French, R. G., Gierasch, P. J., Popp, B. D., and Yerdon, R. J. 1981. Global patterns in cloud forms on Mars. *Icarus* 45:468–493.
- Gaier, J. R., and Perez-Davis, M. E. 1992. *Effect of Particle Size of Martian Dust On the Degradation of Photovoltaic Cell Performance*, NASA TM-105232.
- Gaier, J. R., Perez-Davis, M. E., and Marabito, M. 1990. *Aeolian Removal of Dust from Photovoltaic Surfaces on Mars*, NASA TM-102507.
- Geels, S., Miller, J. B., and Clark, B. C. 1989. Feasibility of using solar power on Mars: Effects of dust storms on incident solar radiation. In *Case for Mars III*,

- ed. C. R. Stoker (San Diego: Univelt), pp. 505–516.
- Greeley, R., and Iversen, J. D. 1985. *Wind as a Geological Process* (Cambridge: Cambridge Univ. Press).
- Green, M. A. 1982. In *Solar Cells: Operating Principles, Technology and System Application* (Englewood Cliffs, N. J.: Prentice-Hall).
- Haberle, R. M., Leovy, C. B., and Pollack, J. B. 1982. Some effects of global dust storms on the atmospheric circulation of Mars. *Icarus* 50:322–367.
- Halpert, G. 1985. The design and application of nickel-cadmium batteries in space. *J. Power Sources* 15:119–140.
- Hanel, R., Conrath, B., Hovis, W., Kunde, V., Lowman, P., Maguire, W., Pearl, J., Pirraglia, H., Prabhakara, C., Schlachman, B., Levin, G., Straat, P., and Burke, T. 1972. Investigation of the Martian environment by infrared spectroscopy on Mariner 9. *Icarus* 17:423–442.
- Hess, S. L., Henry, R. M., Leovy, C. B., Ryan, J. A., and Tillman, J. E. 1977. Meteorological results from the surface of Mars: Viking 1 and 2. *J. Geophys. Res.* 82:4559–4574.
- Hord, S. W., Barth, C. A., and Stewart, A. I. 1972. Mariner 9 ultraviolet spectrometer experiment: Photometry and topography of Mars. *Icarus* 17:443–456.
- Hunt, G. E. 1979. Thermal infrared properties of the martian atmosphere. 4. Predictions of the presence of dust and ice clouds from Viking IRTM spectral measurements. *J. Geophys. Res.* 84:2865–2874.
- Jaquin, F., Gierasch, P., and Kahn, R. 1986. The vertical structure of limb hazes in the Martian atmosphere. *Icarus* 68:442–461.
- Joseph, J. H., Wiscombe, W. J., and Weinman, J. A. 1976. The delta-Eddington approximation for radiative flux transfer. *J. Atmos. Sci.* 28:833–837.
- Kahn, R. 1984. The spatial and seasonal distribution of Martian clouds, and some meteorological implications. *J. Geophys. Res.* 89:6671–6688.
- Kahn, R. 1990. Ice haze, snow, and the Mars water cycle. *J. Geophys. Res.* 95:14677–14694.
- Kahn, R., Goody, R., and Pollack, J. 1981. The martian twilight. *J. Geophys. Res.* 86:5833–5838.
- Kahn, R., Martin, T. Z., Zurek, R. W., and Lee, S. W. 1992. The Martian dust cycle. In *Mars*, eds. H. H. Kieffer, B. M. Jakosky, C. W. Snyder and M. S. Matthews (Tucson: Univ. of Arizona Press), pp. 1017–1053.
- Kieffer, H. H., Martin, T. Z., Peterfreund, A. R., Jakosky, B. M., Miner, E. D., and Palluconi, F. D. 1977. Thermal and albedo mapping of Mars during the Viking primary mission. *J. Geophys. Res.* 82:4249–4291.
- Kuhn, W. R., and Atreya, S. K. 1979. Solar radiation incident on the Martian surface. *J. Molec. Evol.* 14:57–64.
- Landis, G., and Appelbaum, J. 1990. Design considerations for Mars photovoltaic power systems. In *Proc. of 21st IEEE Photovoltaic Specialists Conf.* (New York: Inst. of Electrical and Electronic Engineers), pp. 1263–1270.
- Landis, G., and Appelbaum, J. 1991. Photovoltaic power options for Mars. *Space Power* 10:225–237.
- Leovy, C. B., Briggs, G., Young, A., Smith, B., Pollack, J., Shipley, E., and Wildey, R. 1972. The Martian Atmosphere: Mariner 9 television experiment progress report. *Icarus* 17:373–393.
- Leovy, C. B., Briggs, G. A., and Smith, B. A. 1973. Mars atmosphere during the Mariner 9 extended mission: Television results. *J. Geophys. Res.* 78:4252–4266.
- Linden, D. 1984. *Handbook of Batteries and Fuel Cells* (New York: McGraw-Hill).
- Martin, L. J., and Zurek, R. W. 1993. An analysis of dust activity on Mars. *J. Geophys. Res.*, in press.

- Martin, R. E., Garow, J., and Michaels, K. B. 1984. *Regenerative Fuel Cell Energy Storage System for a Low Earth Orbit Space Station*, NASA CP-174802.
- Martin, T. Z. 1986. Thermal infrared opacity of the Martian atmosphere. *Icarus* 66:2–21.
- McElroy, M. B., and Donahue, T. M. 1972. Stability of the Martian atmosphere. *Science* 177:986–988.
- McKissock, B. I., Kohout, L. L., and Schmitz, P. C. 1990. *A Solar Power System for an Early Mars Expedition*, NASA TM-103219.
- Murphy, J. R., Haberle, R. M., Toon, O. B., and Pollack, J. B. 1993. Martian global dust storms: Zonally symmetric numerical simulations including size dependent particle transport. *J. Geophys. Res.*, in press.
- Owen, T., Biemann, K., Rushneck, D. R., Biller, J. E., Howarth, D. W., and Lafleur, A. L. 1977. The composition of the atmosphere at the surface of Mars. *J. Geophys. Res.* 82:4635–4639.
- Parkinson, T. D., and Hunten, D. M. 1972. Spectroscopy and Aeronomy of O₂ on Mars. *J. Atmos. Sci.* 29:1380–1390.
- Peterfreund, A. P. 1985. Contemporary Aeolian Processes on Mars: Local Dust Storms. Ph. D. Thesis, Arizona State Univ.
- Pollack, J. B., Colburn, D., Kahn, R., Hunter, J., Van Camp, W., Carlston, C., and Wolfe, M. 1977. Properties of aerosols in the martian atmosphere, as inferred from Viking Lander imaging data. *J. Geophys. Res.* 82:4479–4496.
- Pollack, J. B., Colburn, D., Flasar, F. M., Kahn, R., Carlston, C., and Pidek, D. 1979. Properties and effects of dust particles suspended in the martian atmosphere. *J. Geophys. Res.* 84:2929–2945.
- Pollack, J. B., Haberle, R. M., Schaeffer, J., and Lee, H. 1990. Simulations of the general circulation of the martian atmosphere: I. Polar processes. *J. Geophys. Res.* 95:1447–1473.
- Toon, O. B., Pollack, J. B., and Sagan, C. 1977. Physical properties of the particles composing the martian dust storm of 1971–1972. *Icarus* 14:235–244.
- Toulmin, P., III, Baird, A. K., Clark, B. C., Keil, K., Rose, H. J., Jr., Christian, B. P., Evans, P. H., and Kelliher, W. C. 1977. Geochemical and mineralogical interpretation of the Viking inorganic chemical results. *J. Geophys. Res.* 82:4625–4634.
- Van Overstraaten, R. J., and Mertes, R. P. 1986. *Physics Technology and Use of Photovoltaics* (London: Adam Hilger).
- Wells, R. A. 1979. In *Geophysics of Mars* (Amsterdam: Elsevier).
- Zubrin, R. M., Baker, D. A., and Gwynne, O. 1991. Mars Direct: A Simple, Robust, and Cost Effective Architecture for the Space Exploration Initiative. AIAA Paper 91-0326.
- Zurek, R. W. 1981. Inference of dust opacities for the 1977 martian great dust storms from Viking Lander 1 pressure data. *Icarus* 45:202–215.
- Zurek, R. W. 1982. Martian great dust storms: an update. *Icarus* 50:288–310.
- Zurek, R. W., and Martin, L. J. 1993. Interannual variability of planet encircling dust storms on Mars. *J. Geophys. Res.*, in press.